REGENERATION

Meniscal fibrocartilage regeneration inspired by meniscal maturational and regenerative process

Wenqiang Yan[1,2,3], Maihemuti Maimaitimin[1,2,3], Yue Wu[1,2,3], Yifei Fan[1,2,3], Shuang Ren[1,2,3], Fengyuan Zhao[1,2,3], Chenxi Cao[1,2,3], Xiaoqing Hu[1,2,3]*, Jin Cheng[1,2,3]*, Yingfang Ao[1,2,3]*

Meniscus is a complex and crucial fibrocartilaginous tissue within the knee joint. Meniscal regeneration remains to be a scientific and translational challenge. We clarified that mesenchymal stem cells (MSCs) participated in meniscal maturation and regeneration using MSC-tracing transgenic mice model. Here, inspired by meniscal natural maturational and regenerative process, we developed an effective and translational strategy to facilitate meniscal regeneration by three-dimensionally printing biomimetic meniscal scaffold combining autologous synovium transplant, which contained abundant intrinsic MSCs. We verified that this facilitated anisotropic meniscus–like tissue regeneration and protected cartilage from degeneration in large animal model. Mechanistically, the biomechanics and matrix stiffness up-regulated Piezo1 expression, facilitating concerted activation of calcineurin and NFATc1, further activated YAP-pSmad2/3-SOX9 axis, and consequently facilitated fibrochondrogenesis of MSCs during meniscal regeneration. In addition, Piezo1 induced by biomechanics and matrix stiffness up-regulated collagen cross-link enzyme expression, which catalyzed collagen cross-link and thereby enhanced mechanical properties of regenerated tissue.

INTRODUCTION

Menisci, the semilunar wedge-shaped fibrocartilage tissue provided structural congruency between distal femur and proximal tibia and absorbed mechanical shock during knee joint motion (*1*). Because of poor, intrinsic healing capacity of menisci, meniscectomy was the prevailing therapy (*2*). Without the mechanical absorption of menisci, the hyaline cartilage in femur and tibia was exposed to excessive biomechanics, a critical predisposing factor of cartilage degeneration or even osteoarthritis (*3*). To date, several types of meniscal substitutes have been developed to replace native menisci, aiming to decrease joint cartilage degeneration (*4*). Among them, meniscal allograft transplantation has been performed in clinic for several decades. However, the issues of limited graft availability, immune rejection, disease transmission, and unsatisfactory long-term chondroprotection could not be ignored (*5*, *6*). Another two synthetic substitutes including collagen meniscus implant (Stryker Corporation, Kalamazoo, MI, USA) and polyurethane polymeric implants (Actifit, Orteq Sports Medicine Ltd., London, UK) have been approved for clinical use and yielded satisfactory patient reported outcomes (*7*, *8*). However, the reported adverse events including graft shrinkage, myxoid degeneration, and problematic integration with host tissue could not be neglected (*6*). Recently, the anisotropic meniscal tissue resembling native menisci has been constructed using tissue engineering strategies (*9*, *10*), which would be a promising meniscal substitute in the future.

There are several obstacles that limit the translation of tissue-engineered menisci into clinic. First, the seeding cells used for meniscal tissue engineering mainly include mesenchymal stem cells (MSCs), meniscal fibrochondrocytes, or chondrocytes (*1*, *4*). However, the tumorigenicity of MSCs and immune rejection of allogenic cells could not be ignored (*1*, *11*). Autologous cell transplantation also encountered adverse events including extra injury to donor site during cell harvesting and dedifferentiation during in vitro culture (*1*). In the present study, we identified that MSCs participated in maturation and regeneration of menisci using an MSC-tracing transgenic mice model, which had robust healing capacity (*12*). Previous studies have used synovial tissue transplant to repair meniscal injury or regenerate meniscal tissue (*13*–*16*). The synovium contained abundant intrinsic MSCs and would be an ideal cell source that contributed to meniscal regeneration due to the superior chondrogenic capacity than other mesenchymal tissue–derived stem cells (*17*, *18*). Moreover, previous studies have demonstrated that the synovium-derived MSCs (SMSCs) facilitated the repair and regeneration of meniscus (*19*, *20*). Thereby, autologous synovium transplantation not only provided reparative cells but also avoided the aforementioned adverse events caused by cell transplantation. Second, the biochemical stimulus was a critical factor that induced or maintained fibrochondrogenic phenotype of reparative cells during meniscal regeneration. The growth factors such as transforming growth factor–β (TGFβ) family members, fibroblast growth factors, connective tissue growth factor (CTGF), and so on were most commonly used and effective in inducing fibrochondrogenesis and promoting extracellular matrix deposition (*1*). However, the dose, release model, metabolism, pharmacokinetics, and immunogenicity in vivo could not be defined. We found that the synovium was rich in TGFβ and CTGF in the present study, which would provide biochemical stimuli for meniscal regeneration. Third, the menisci functioned under joint compression conditions; thereby, biomechanical stimulation was important for meniscal regeneration and remodeling (*4*). Several studies used compressive bioreactor to provide compression stimulus in vitro, aiming to simulate native joint compression (*9*, *21*, *22*). The anisotropy of mechanical property and matrix production of

[1]Department of Sports Medicine, Peking University Third Hospital, Institute of Sports Medicine of Peking University, Beijing, China. [2]Beijing Key Laboratory of Sports Injuries, Beijing, China. [3]Engineering Research Center of Sports Trauma Treatment Technology and Devices, Ministry of Education, Beijing, China.
*Corresponding author. Email: aoyingfang@163.com (Y.A.); chengjin@bjmu.edu.cn (J.C.); huxiaoqingbd01@sina.com (X.H.)

engineered menisci could be improved by in vitro compression stimulus. However, the optimal intensity, frequency, and period of in vitro compression stimulus could not be defined, which may result in inconsistent results. Naturally, the biomechanical stimulus generated by native joint compression would be optimal for meniscal regeneration and remodeling.

Here, inspired by meniscal natural maturational and regenerative process, we developed an effective and translational strategy to facilitate meniscal regeneration by three-dimensionally (3D) printing biomimetic meniscal scaffold combining autologous synovium transplant. The degree of meniscal regeneration and chondroprotection was evaluated after subtotal meniscectomy [90% excision, a relatively serious operation for meniscal injuries (*23*)] in a porcine large animal model, which had limited repair capacity similar to human beings (*12*, *24*). The potential mechanisms of meniscal regeneration and remodeling were also clarified.

RESULTS

MSCs participated in maturation and regeneration of mice meniscus

To identify the role of MSCs in maturation of native meniscus, the *Pdgfrα-CreER*; *Rosa26-LSL-Tdtomato* MSC-tracing transgenic mice were applied. The platelet-derived growth factor α (Pdgfrα)–positive MSCs expressed tdtomato protein [one kind of red fluorescence protein (RFP)]. The induction with tamoxifen was started at 8 weeks after birth for 1 week. The knee joint was harvested at 10 weeks after birth (Fig. 1A). The immunofluorescence costaining demonstrated that RFP/SOX9/collagen I (COL I)/COL II–positive cells were present in native menisci (Fig. 1, B and C). This indicated that the cells expressing MSC marker *pdgfrα* between 8 and 10 weeks after birth differentiated into meniscal fibrochondrocytes. Using the same knee joint tissue, the pdgfrα/SOX9/COL I/COL II–positive cells could be observed in native menisci (Fig. 1, D and E). This indicated that MSCs were still present in native menisci at 10 weeks after birth. Thus, MSCs participated in maturation of native mice menisci. Previous studies have demonstrated that small animal models, such as mice, had relatively robust intrinsic healing capacity (*25*). Small animals could be an appropriate model to study the native healing process of meniscus. To examine the role of MSCs in meniscal regeneration, after the induction of *Pdgfrα-CreER*; *Rosa26-LSL-Tdtomato* transgenic mice, total meniscectomy or anterior half partial meniscectomy of medial menisci was performed. At 3 months postoperatively, the regenerated meniscal fibrocartilage–like tissue rich in glycosaminoglycans (GAGs), COL I, and COL II was identified by histological staining (Fig. 1, F and G). Moreover, the RFP/COL I/COL II/SOX9–positive cells were present in the regenerated tissue (Fig. 1, G and H). This indicated that MSCs participated in the regeneration of menisci and differentiated into meniscal fibrochondrocytes. In conclusion, these results suggested that MSCs participated in maturation and regeneration of mice meniscus.

3D printing PCL scaffold combining autologous synovium transplant facilitated meniscal regeneration and protected cartilage in large animal model

The detailed protocol for scaffold 3D printing was described in the Supplementary Materials. To validate the effect of autologous synovium transplant on meniscal regeneration, a subtotal meniscectomy (90% excision) model in minipig was used. First, subtotal meniscectomy was performed in medial meniscus (Fig. 2, A1). Second, a 3D-printed poly-ε-caprolactone (PCL) meniscal scaffold was transplanted anatomically and fixed with the residual meniscal tissue with sutures (Fig. 2, A2). Third, autologous synovial tissue was harvested from suprapatellar bursa and spread on the surface of scaffold (Fig. 2A3). Last, all joint structures were restored anatomically (Fig. 2A4). To track meniscal regeneration and cartilage status, the minimal invasive arthroscopic examination was performed at 2 months postoperatively (Fig. 2B1). After comprehensive evaluation, no loose bodies were observed in joint cavity, and the meniscal scaffold demonstrated intact and secured fixation in anatomical position. Moreover, the whole meniscal scaffold was covered with newly formed tissue, which was abundant in blood vessels (Fig. 2B2). To further evaluate the content of newly formed tissue and cartilage status, the samples were harvested at 2 months postoperatively. Generally, the regenerated tissue was similar to native menisci in terms of wedge-shaped morphology and color. The regenerated tissue demonstrated good coverage on tibial cartilage and good connectivity with peripheral capsule. Moreover, anterior and posterior attachment on tibial plateau still remained superior (Fig. 2, C1 to C3). For cartilage status, only mild cartilage wear was present in medial tibial plateau and medial femoral condyle (MFC). No cartilage degeneration was observed in patellofemoral joint (Fig. 2, C4 to C7). The bone block of medial collateral ligament upper attachment site healed well (Fig. 2C8). At 4 months postoperatively, the regenerated tissue was more like native menisci. Moderate cartilage abrasion was present in medial tibial plateau. Only mild cartilage wear was observed in MFC. The cartilage status in patellofemoral joint still remained normal (Fig. 2D). In sham group, all joint structures remained normal, which indicated no adverse effects caused by operation (Fig. 2E). In contrast, for subtotal meniscectomy group, only partial soft tissue attached to the residual meniscal tissue. Obvious cartilage degeneration was observed (fig. S1, A and B). For blank PCL scaffold group, some irregular and soft tissue could be observed in the scaffold. Cartilage erosion and defect could be observed. The bone block of medial collateral ligament upper attachment site healed well (fig. S1, C and D).

To evaluate the histomorphology of meniscus tissue comprehensively, the meniscus tissue was divided into three parts from anterior to posterior, including anterior horn, body, and posterior horn (Fig. 3A1). The inner, middle, and outer zones of each part were analyzed (Fig. 3A2). For subtotal meniscectomy group, only some loose fibrous and fibrovascular tissue with fewer GAGs was observed. The cellular content was mainly composed of spindle-shaped fibroblast-like cells. Some blood vessels could be observed (Fig. 3, B1 and B2). For blank PCL scaffold group, some fibrous, fibrovascular, and less fibrocartilaginous tissue was observed within the scaffold. The newly formed tissue had poor integration with peripheral residual meniscal tissue. The cellular content contained some spindle-shaped fibroblast-like cells and fewer oval- to round-shaped chondrocyte-like cells. Blood vessels were observed in the regenerated tissue. The PCL material remnants existed at 4 months postoperatively (Fig. 3, B3 and B4). For PCL scaffold + synovium transplant group, the histological outcomes showed the formation of less fibrous, fibrovascular, and more fibrocartilaginous matrix, demonstrating variable amounts of collagen and GAG-rich matrix. The regenerated tissue was populated by spindle-shaped fibroblast-like cells and more oval to round-shaped chondrocyte-like

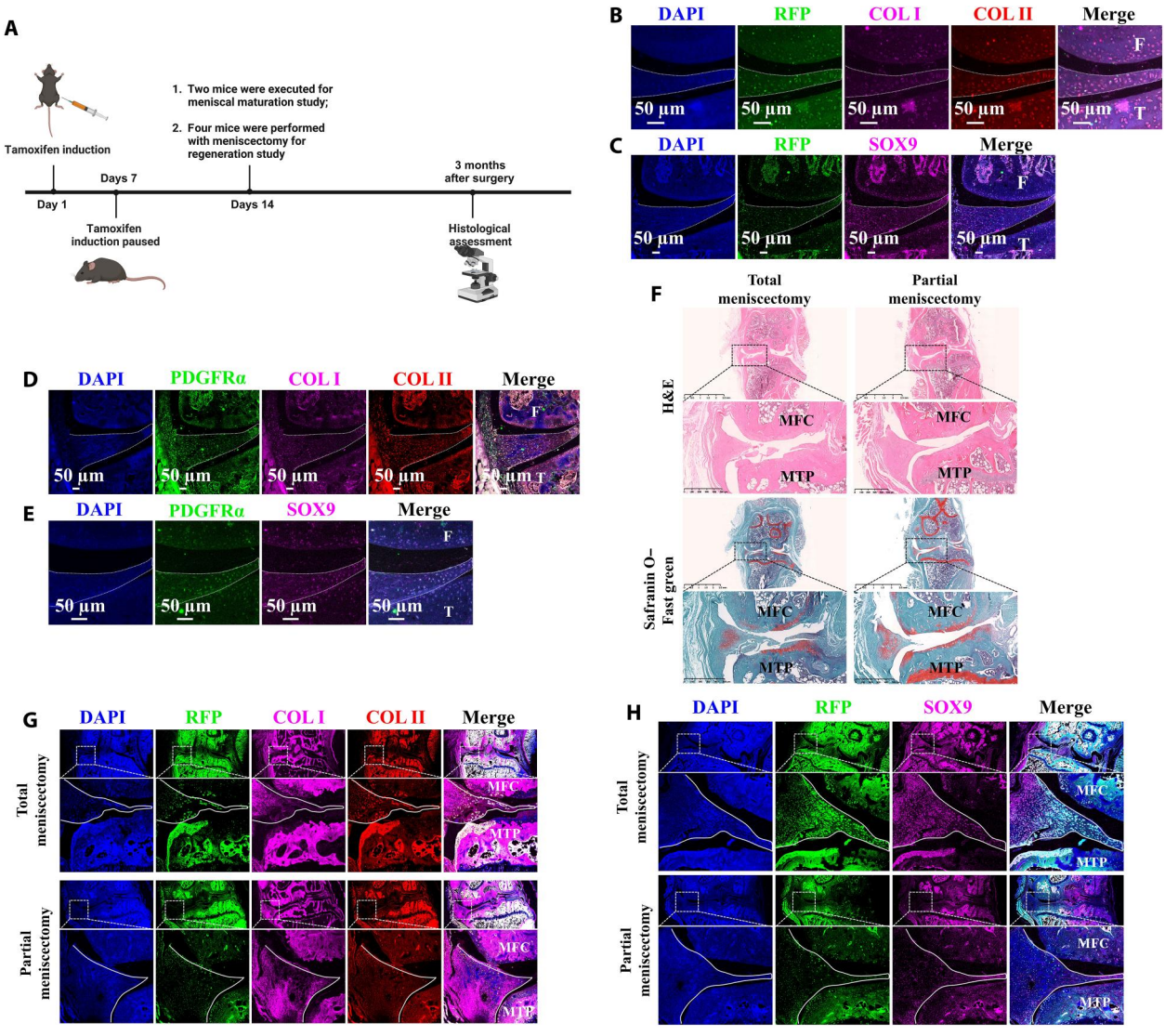

Fig. 1. MSCs participate in meniscal maturation and regeneration verified by MSCs tracing transgenic mice. (**A**) Schematic diagram. (**B**) Immunofluorescent costaining of RFP, COL I, and COL II of mice native meniscus after tamoxifen induction. F, femur; T, tibia. (**C**) Immunofluorescent costaining of RFP and SOX9 of mice native meniscus after tamoxifen induction. (**D**) Immunofluorescent costaining of PDGFRα, COL I, and COL II of mice native meniscus after tamoxifen induction. (**E**) Immunofluorescent costaining of PDGFRα and SOX9 of mice native meniscus after tamoxifen induction. (**F**) Histological assessment of mice meniscal regeneration after total or partial meniscectomy. (**G**) Immunofluorescent costaining of RFP, COL I, and COL II in mice regenerated meniscus after tamoxifen induction. The solid white lines represent the contour of regenerated meniscus. MFC, medial femoral condyle; MTP, medial tibial plateau. (**H**) Immunofluorescent costaining of RFP and SOX9 in mice regenerated meniscus after tamoxifen induction. H&E, hematoxylin and eosin. DAPI, 4′,6-diamidino-2-phenylindole.

cells. Blood vessels were observed in the regenerated tissue. The PCL material remnants still existed at 4 months postoperatively. As demonstrated by Safranin O staining, the matrix in regenerated tissue was rich in GAG, especially in the inner and middle zones similar to native porcine menisci (Fig. 3, B5 to B8). Next, we evaluated the deposition of COL I and COL II in the regenerated tissue. For PCL scaffold + synovium transplant group, the regenerated tissue was abundant in COL I and COL II. COL II matrix was mainly distributed in the inner and middle zone of regenerated tissue resembling native menisci, demonstrating anisotropic distribution of COL II. The whole tissue was rich in COL I but mainly distributed in the middle and outer zone similar to native meniscus, indicating anisotropic distribution of COL I. Moreover, the collagen (COL I and COL II) content at 4 months postoperatively increased compared to that of 2 months postoperatively and resembled native menisci. However, the subtotal meniscectomy group and blank PCL scaffold group had less COL I and COL II compared to those of PCL scaffold + synovium transplant group. The characteristic anisotropy of collagen distribution was absent (Fig. 3C and figs. S2 to S10). Moreover, for PCL scaffold + synovium transplant group, the regenerated tissue was abundant in aggrecan. The aggrecan matrix had the trend to be mainly distributed in the inner and middle zones similar to native menisci, demonstrating anisotropic distribution of aggrecan. For aggrecan semiquantitative analysis, there was substantial difference in aggrecan content between the inner and outer zones of regenerated tissue in PCL scaffold +

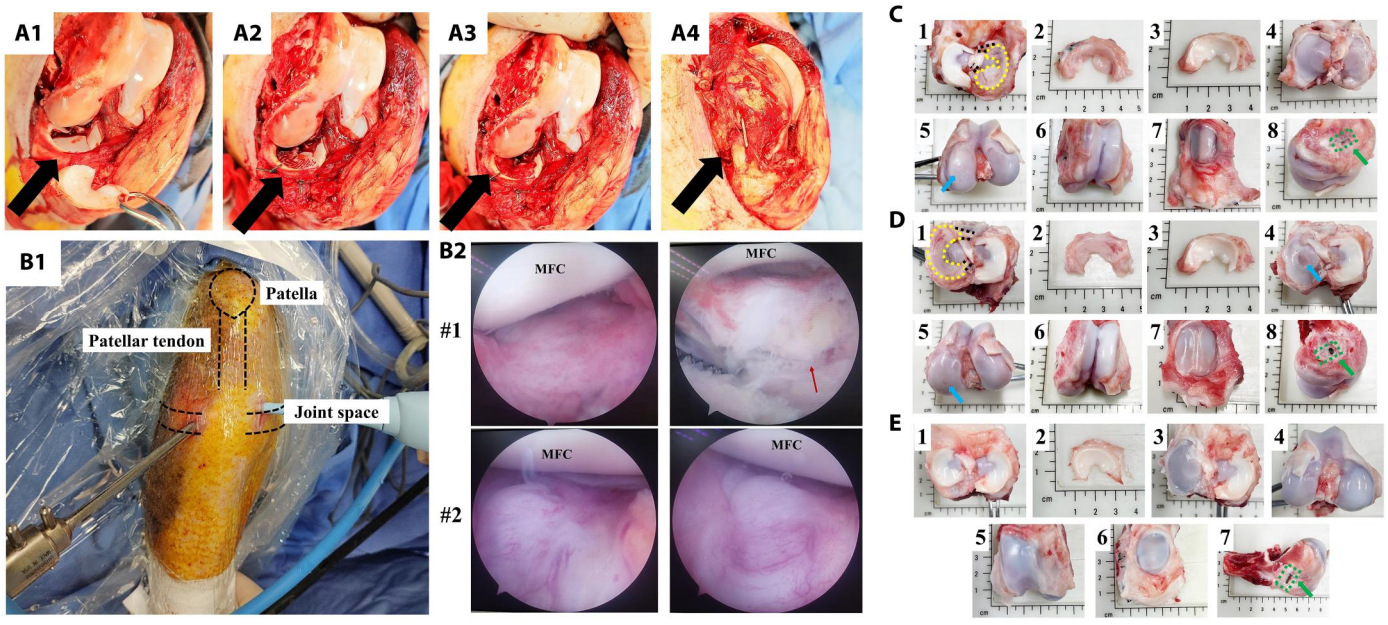

Fig. 2. 3D printing meniscal scaffold combining autologous synovium transplant facilitates meniscal regeneration and protects cartilage from macroscopic view in porcine subtotal meniscectomy model. (**A**) 3D printing meniscal scaffold combining autologous synovium transplantation after preparation of subtotal meniscectomy in porcine medial meniscus [(A1) the preparation of subtotal meniscectomy in medial meniscus, black arrow represents medial meniscus; (A2) meniscal scaffold is transplanted anatomically and fixed with peripheral residual meniscal tissue using sutures; (A3) autologous synovium is harvested from suprapatellar bursa and covered on the surface of scaffold; (A4) the bone block of medial collateral ligament upper attachment site is fixed anatomically using nail, black arrow represents medial collateral ligament]. (**B**) Arthroscopic examination of knee joint of PCL scaffold + synovium transplant group at 2 months postoperatively [(B1) the performance of arthroscopic examination; (B2) joint conditions under arthroscope, red arrow represents PCL scaffold, MFC, medial femoral condyle]. (**C**) The macroscopic appearance of regenerated tissue and cartilage status of PCL scaffold + synovium transplant group at 2 months postoperatively (1, the regenerated tissue located in the tibia, black dotted lines represent anterior and posterior attachment ligament, yellow dotted line represents contour of regenerated tissue; 2, the regenerated tissue; 3, native meniscus; 4, the tibial plateau cartilage; 5, the femoral condyle cartilage, blue arrow represents cartilage wear; 6, cartilage in the trochlea; 7, cartilage in the patella; 8, good bone healing of medial collateral ligament upper attachment site as indicated by green arrow). (**D**) Macroscopic appearance of regenerated tissue and cartilage status of PCL scaffold + synovium transplant group at 4 months postoperatively. (**E**) Macroscopic appearance of knee joint of sham group at 4 months postoperatively.

synovium-2 M goup. The aggrecan content of regenerated tissue resembled that of native menisci. However, the subtotal meniscectomy group and blank PCL scaffold group contained less aggrecan compared to that of PCL scaffold + synovium transplant group. The characteristic anisotropy of aggrecan distribution was not observed (Fig. 3D and figs. S11 to S18). We also characterized the pericellular matrix (PCM) (perlecan and COL VI), which was critical for meniscal fibrochondrocytes in mechanobiology (*26*). The regenerative cells in PCL scaffold + synovium transplant group were surrounded by abundant perlecan and COL VI, resembling those of native meniscal fibrochondrocytes. However, the PCM (perlecan and COL VI) of regenerative cells in subtotal meniscectomy group and blank PCL scaffold group was inferior in content and area compared to those of PCL scaffold + synovium transplant group (Fig. 3E and fig. S19).

Then, we evaluated collagen content within regenerated tissue using two-photon microscopy. The collagen content of regenerated tissue in PCL scaffold + synovium transplant group was superior compared to that of subtotal meniscectomy group and blank PCL scaffold group and was closer to that of native meniscus (fig. S20A). We also analyzed the arrangement of collagen fibers using Sirius red staining. The collagen fiber orientation within regenerated tissue of PCL scaffold + synovium transplant group resembled that of native menisci (fig. S20B). The reduced modulus of native meniscus and regenerated tissue was evaluated. The regenerated tissue of subtotal meniscectomy group and blank PCL scaffold group was too soft to be measured. Thus, only the data of native meniscus and PCL scaffold + synovium transplant group were shown. In anterior portion, the reduced modulus of PCL scaffold + synovium transplant group 4M (11.39 ± 1.05 MPa) was superior to that of PCL scaffold + synovium transplant group 2M (3.72 ± 0.98 MPa) and resembled that of native meniscus (18.80 ± 3.03 MPa). In the middle portion, the reduced modulus of PCL scaffold + synovium transplant group 4M (12.82 ± 1.73 MPa) was superior to that of PCL scaffold + synovium transplant group 2M (5.29 ± 0.77 MPa) and close to that of native meniscus (29.33 ± 5.29 MPa). In the posterior portion, identically, the reduced modulus of PCL scaffold + synovium transplant group 4M (19.34 ± 1.57 MPa) was superior to that of PCL scaffold + synovium transplant group 2M (8.93 ± 0.76 MPa) and close to that of native meniscus (35.25 ± 4.19 MPa) (fig. S20C). In addition, no COL10A1 was present in regenerated tissue and native menisci, which indicated no hypertrophy (fig. S20D). The angiography showed that the regenerated tissue of PCL scaffold + synovium transplant group was rich in blood vessels at 2 months postoperatively. The blood vessel content decreased significantly at 4 months postoperatively. Moreover, the blood supply was only present in the peripheral rim of native menisci (fig. S20E). The cartilage histology showed that the PCL scaffold + synovium transplant group

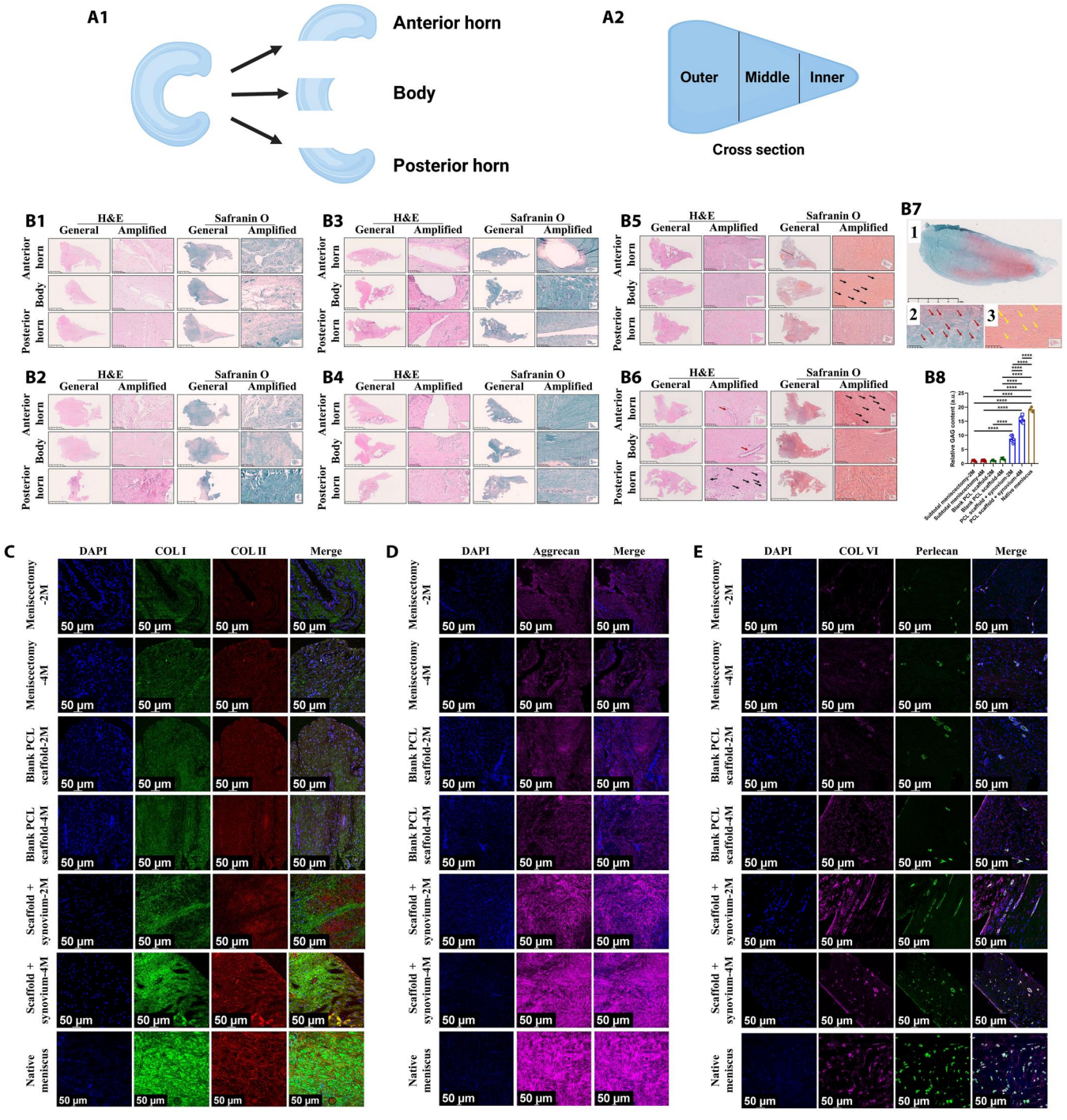

Fig. 3. 3D printing scaffold combining autologous synovium transplant facilitates anisotropic meniscal regeneration from histological view in porcine subtotal meniscectomy model. (**A**) Schematics of meniscus segmentation for subsequent histological analysis [(A1) from anterior to posterior, meniscus tissue is divided into anterior horn, body, and posterior horn; (A2) from inner to outer, meniscus tissue is divided into inner, middle, and outer zones]. (**B**) Histological analysis of regenerated tissue and native meniscus [(B1) subtotal meniscectomy group, 2 months; (B2) subtotal meniscectomy group 4 months; (B3) blank PCL scaffold group 2 months; (B4) blank PCL scaffold group 4 months; (B5) PCL scaffold + synovium transplant group 2 months, black arrows represent regenerative fibrochondrocyte-like cells; (B6) PCL scaffold + synovium transplant group 4 months, black arrows represent regenerative fibrochondrocyte-like cells, red arrows represent blood vessels; (B7) Safranin O–fast green staining of native menisci, 1, Safranin O–fast green staining; 2, red arrows represent native meniscal fibrochondrocytes; 3, yellow arrows represent regenerative fibrochondrocyte-like cells in regenerated tissue of PCL scaffold + synovium transplant group; (B8) the semiquantitative assessment of GAG, 2M, 2 months postoperatively; 4M, 4 months postoperatively; $n = 3$ for native meniscus; $n = 6$ for other groups; one-way analysis of variance (ANOVA)]. (**C**) Representative images of COL I and COL II immunofluorescence in regenerated tissue and native meniscus. (**D**) Representative images of aggrecan immunofluorescence in regenerated tissue and native meniscus. (**E**) Representative images of perlecan and COL VI immunofluorescence in regenerated tissue and native meniscus. ****$P < 0.0001$; a.u., arbitrary units.

demonstrated less cartilage abrasion, proteoglycan loss, and lower osteoarthritis cartilage histopathology assessment system (OARSI) scores compared to subtotal meniscectomy group and blank PCL scaffold group (fig. S20F). The minipig of PCL scaffold + synovium transplant group was recovered to normal gait at 2 and 4 months postoperatively (movies S4 and S5).

Biomechanical stimulus promoted MSCs chondrogenesis through YAP-pSmad2/3-SOX9 axis

In the present study, we first identified the differentiation of MSCs into fibrochondrocytes in regenerated tissue of PCL scaffold + synovium transplant group. The porcine MSC marker CD90 (*27*) was identified in the synovium of normal, PCL scaffold + synovium transplant group (2 and 4 months postoperatively) (fig. S21A1). The synovial hyperplasia was present after operation. The quantities of total synovial cells and MSCs increased significantly at 2 and 4 months postoperatively (fig. S21A2). The CD90/SOX9/COL I/COL II–positive cells were observed in regenerated tissue of PCL scaffold + synovium transplant group, which demonstrated the differentiation of MSCs into fibrochondrocytes during regeneration (fig. 21, B and C). The CD90-positive rate in regenerated tissue of PCL scaffold + synovium transplant group decreased significantly at 4 months compared to that of 2 months (fig. S21B3). Moreover, the CD90/SOX9/COL I/COL II–positive cells could also be observed in native porcine menisci (fig. S21D). Second, we hypothesized that the biomechanical stimulus promoted the chondrogenesis of MSCs. The molecular mechanism in vitro was explored using SMSCs derived from human beings. To simulate the biomechanical stimulation on human SMSCs, the cyclic tensile strain was applied in vitro. Previous study demonstrated that a mean 5% strain was present in native menisci at 100% weight-bearing condition (*28*). Then, a periodic 5% strain for 4 hours was applied on human SMSCs using in vitro Flexcell train culture system. To identify the underlying gene expression changes, we performed RNA sequencing (RNA-seq) analyses in human SMSCs samples treated with 5% strain or static. The genes were differentially expressed after Flexcell treatment (Fig. 4A1). Moreover, the Kyoto Encyclopedia of Genes and Genomes (KEGG) pathway analysis revealed that the Hippo signaling pathway and TGFβ signaling pathway were involved (Fig. 4A2). In addition, we performed RNA-seq analyses in the samples of regenerated tissue of PCL scaffold + synovium transplant group and native porcine menisci. The differentially expressed genes were present between regenerated tissue and native porcine menisci (Fig. 4, B1 to B3 and C1 to C3). The KEGG pathway analysis also revealed that the Hippo signaling pathway and TGFβ signaling pathway were involved (Fig. 4, D1 to D3). Then, the key targets of Hippo, TGFβ signaling pathway, and fibrochondrogenic phenotype were evaluated by Western blot, quantitative real-time polymerase chain reaction (qPCR), and cell immunofluorescence. After CTS treatment in human SMSCs, for Hippo signaling pathway, total YAP (Yes-associated protein 1) mRNA and protein were up-regulated; the downstream target genes of YAP including CCN1, CTGF, and BIRC5 were all up-regulated, whereas pYAP (phosphorylated YAP) was down-regulated, indicating YAP nuclear translocation. For TGFβ signaling pathway, pSmad2/3 (phosphorylated Smad2/3) was up-regulated. For fibrochondrogenesis, COL II and aggrecan were up-regulated significantly, while COL I was down-regulated, and SOX9 had no significant changes (Fig. 4, E and F). Previous study demonstrated that YAP dictated the localization of Smad2/3 by forming YAP-Smad2/3 complexes (*29*). Moreover, Smad3 could enhance SOX9-dependent transcriptional activation in primary chondrogenesis by forming Smad3/CBP/p300/SOX9 complexes (*30*). Therefore, we hypothesized that biomechanical stimulation–induced YAP nuclear translocation could enhance Smad3-induced SOX9 transcriptional activity. Then, the dihydrexidine reagent to promote YAP phosphorylation (cytoplasmic translocation) or SIS3 reagent to inhibit phosphorylation of Smad3 were performed to identify the YAP-pSmad2/3-SOX9 axis in MSC chondrogenesis. pYAP expression was up-regulated when human SMSCs were treated with dihydrexidine, while pSmad2/3, SOX9, COL II, and GAG were down-regulated. The expression of pSmad2/3 was down-regulated when treated with SIS3. Moreover, SOX9, COL II, and GAG were down-regulated. Total YAP protein was down-regulated, while pYAP was up-regulated after SIS3 treatment. These findings may be attributed to the following reasons. First, SIS3 treatment inhibited phosphorylation of Smad3, thus leading to cytoplasmic translocation of Smad3. Second, previous study demonstrated that pYAP binds SMAD complexes in the cytoplasm (*29*). Last, the accumulation of Smad3 in cytoplasm sequestrated YAP in the cytoplasm, which opposed the effect of CTS treatment. Subsequent protein degradation occurred in pYAP, thus leading to loss of YAP protein (Fig. 5A). Thus, the biomechanics-induced YAP-pSmad2/3-SOX9 axis promoted primary chondrogenesis of human SMSCs.

As aforementioned, the Hippo and TGFβ signaling were enriched in porcine-regenerated tissue of PCL scaffold + synovium transplant group. Then, we analyzed key targets of Hippo and TGFβ signaling in porcine-regenerated tissue. First, the regenerative cells were rich in YAP and pYAP. The expression of YAP was up-regulated at 4 months postoperatively compared to that of 2 months (fig. S22A), whereas pYAP decreased significantly at 4 months postoperatively (fig. S22B). Moreover, YAP and pYAP could be observed in native porcine meniscal fibrochondrocytes (fig. S22, C and D). Second, we observed that the preoperative normal porcine synovium and postoperative synovium of PCL scaffold + synovium transplant group were abundant in TGFβ1 and CTGF growth factors (fig. S22E). Previous studies have demonstrated that TGFβ and CTGF facilitated fibrochondrogenesis of MSCs, synergistically (*9*, *10*). We also identified the fibrochondrogenic differentiation of human SMSCs seeded onto PCL scaffold when treated with TGFβ1 and CTGF synergistically (fig. S22F, G and H). Subsequently, we found that the regenerated tissue of PCL scaffold + synovium transplant group contained TGFβ1 and CTGF (fig. S22, I1 and I2), resembling native porcine menisci (fig. S22, I3 and I4). The regenerative cells of PCL scaffold + synovium transplant group and native porcine meniscal fibrochondrocytes demonstrated positive pSmad2/3 (fig. S22J). Moreover, the expression of pSmad2/3 in synovium of PCL scaffold + synovium transplant group increased compared to that of normal porcine synovium (fig. S22K). Next, we evaluated the interactions between Hippo and TGFβ signaling pathway in regenerative cells of PCL scaffold + synovium transplant group. The outcomes of immunofluorescent colocalization demonstrated that YAP and Smad2/3 interacted closely, with high overlap coefficient (Fig. 5B). In addition, pSmad2/3 and SOX9 also had close interactions, with high overlap coefficient (Fig. 5C). Thus, we identified the critical role of YAP-pSmad2/3-SOX9 axis in the chondrogenesis of SMSCs and subsequent meniscal regeneration.

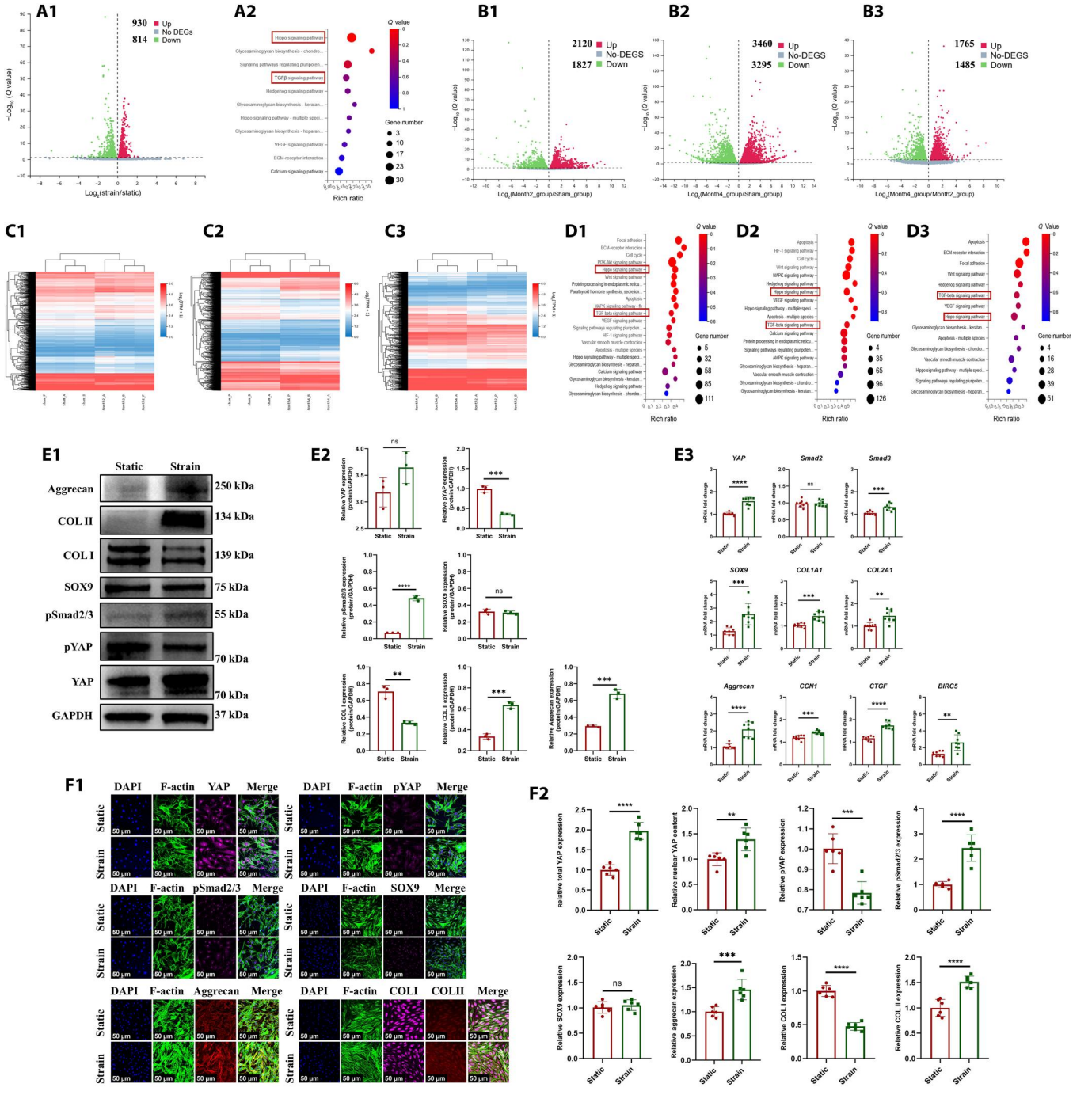

Fig. 4. The identification of YAP-pSmad2/3-SOX9 axis during MSCs chondrogenesis. (**A**) RNA-seq analyses in human SMSCs after static and CTS treatment [(A1) volcano plot of differentially expressed genes (DEGs) in CTS group versus static group; (A2) KEGG pathway enrichment, red boxes represent Hippo and TGFβ signaling]. (**B**) Volcano plot of differentially expressed genes in regenerated tissue of PCL scaffold + synovium transplant group versus native porcine menisci [(B1) PCL scaffold + synovium transplant group 2M versus native menisci of sham group; (B2) PCL scaffold + synovium transplant group 4M versus native menisci of sham group; (B3) PCL scaffold + synovium transplant group at 2 versus 4 months]. (**C**) Heatmap of differential gene cluster in regenerated tissue of PCL scaffold + synovium transplant group and native porcine menisci [(C1) PCL scaffold + synovium transplant group 2M versus native menisci of sham group; (C2) PCL scaffold + synovium transplant group 4M versus native menisci of sham group; (C3) PCL scaffold + synovium transplant group at 2 versus 4 months]. (**D**) KEGG pathway enrichment in regenerated tissue of PCL scaffold + synovium transplant group and native porcine menisci [(D1) PCL scaffold + synovium transplant group 2M versus native menisci of sham group; (D2) PCL scaffold + synovium transplant group 4M versus native menisci of sham group; (D3) PCL scaffold + synovium transplant group at 2 versus 4 months, the red boxes represent Hippo and TGFβ signaling]. (**E**) Protein and mRNA levels in human SMSCs after static and CTS treatment [(E1) Western blot analysis; (E2) semiquantitative analysis of Western blot, $n = 3$, unpaired t test; (E3) mRNA levels, $n = 8$, unpaired t test]. (**F**) Cell immunofluorescence of human SMSCs after static and CTS treatment [(F1) cell immunofluorescence; (F2) six regions are randomly selected for semiquantitative analysis; the intensity of immunofluorescence is calculated by ImageJ software, $n = 6$, unpaired t test] (continued with Fig. 5). $^{**}P < 0.01$, $^{***}P < 0.0005$, $^{****}P < 0.0001$; ns, not significant.

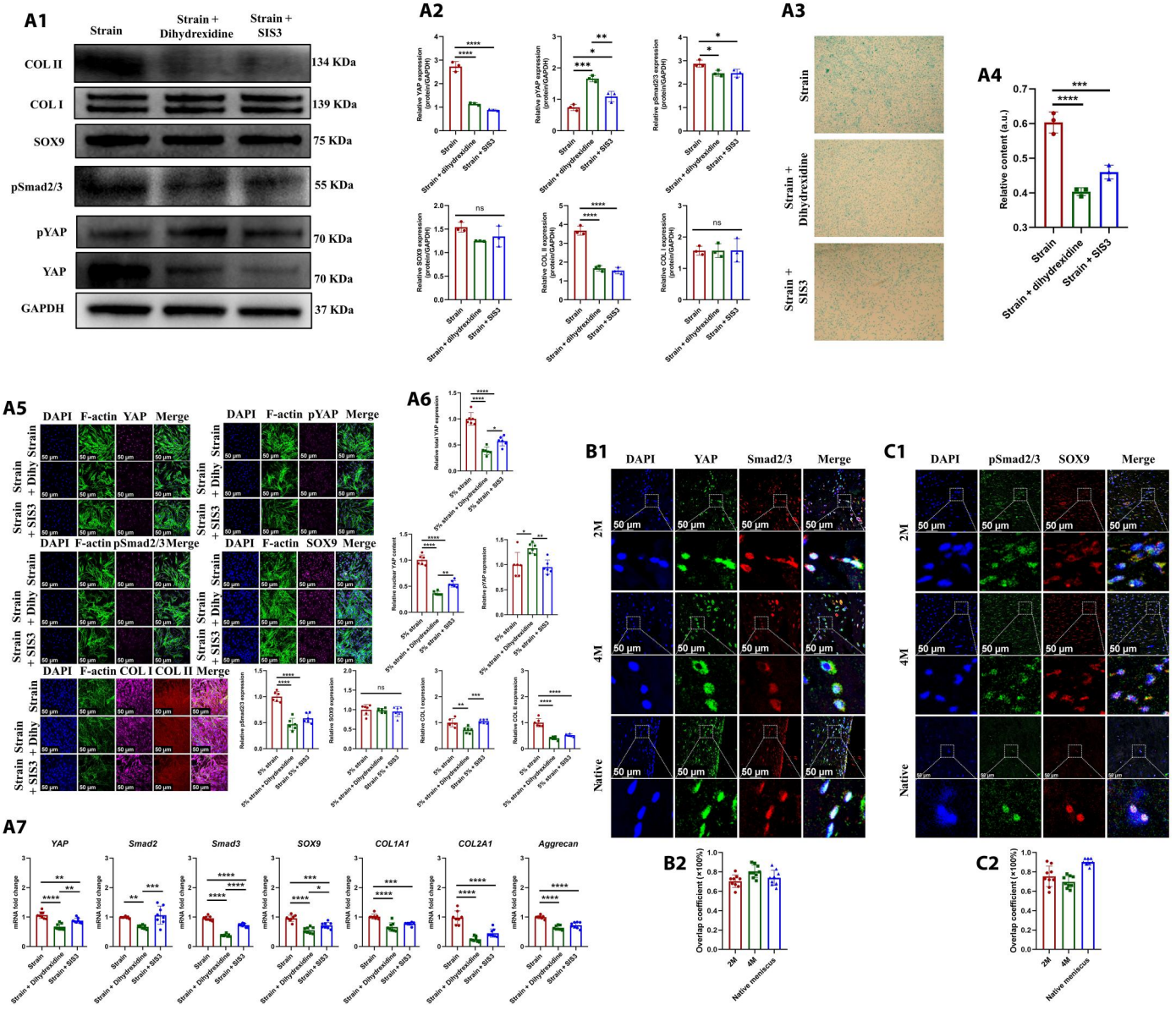

Fig. 5. The identification of YAP-pSmad2/3-SOX9 axis during MSCs chondrogenesis. (**A**) Protein and mRNA levels in human SMSCs after being treated with dihydrexidine and SIS3 [(A1) the Western blot analysis; (A2) the semiquantitative analysis of Western blot, $n = 3$, one-way ANOVA; (A3) the alcian blue staining; (A4) the semiquantitative analysis of alcian blue staining, $n = 3$, one-way ANOVA; (A5) cell immunofluorescence; (A6) the semiquantitative analysis of cell immunofluorescence, Dihy represents dihydrexidine, $n = 6$, one-way ANOVA; (A7) the mRNA levels, $n = 8$, one-way ANOVA]. (**B**) Immunofluorescent colocalization of YAP and Smad2/3 in regenerated tissue of PCL scaffold + synovium transplant group and native porcine menisci [(B1) immunofluorescent colocalization of YAP and Smad2/3; (B2) immunofluorescence overlap coefficient, $n = 9$]. (**C**) Immunofluorescent colocalization of pSmad2/3 and SOX9 in regenerated tissue of PCL scaffold + synovium transplant group and native porcine menisci [(C1) immunofluorescent colocalization of pSmad2/3 and SOX9; (C2) immunofluorescence overlap coefficient, $n = 9$]. $^{*}P < 0.05$, $^{**}P < 0.01$, $^{***}P < 0.0005$, $^{****}P < 0.0001$; ns, not significant.

Piezo1 mediated mechanotransduction through concerted activation of calcineurin and NFAT

As aforementioned, we have identified that the biomechanical stimulus could promote MSC chondrogenesis through YAP-pSmad2/3-SOX9 axis. It was hypothesized that some direct mechanical response molecule in the upstream mediated mechanotransduction. Previous studies have demonstrated that the mechanosensitive ion channel Piezo1 participated in the homeostasis and repair of musculoskeletal systems, including cartilage, bone, skeletal muscle, tendon, and intervertebral disc (*31*). The aforementioned KEGG pathway analysis revealed that calcium signaling pathway was enriched in human SMSCs after CTS treatment (Fig. 4A2) and porcine-regenerated tissue of PCL scaffold + synovium transplant group (Fig. 4, D1 and D2). While, the mechanosensitive Piezo1 channel was the known Ca^{2+} permeable channel (*32*). Here, we hypothesized that Piezo1 was the upstream of YAP-pSmad2/3-SOX9 axis. First, we found that the protein and mRNA level of Piezo1 was up-regulated significantly in human SMSCs after CTS treatment

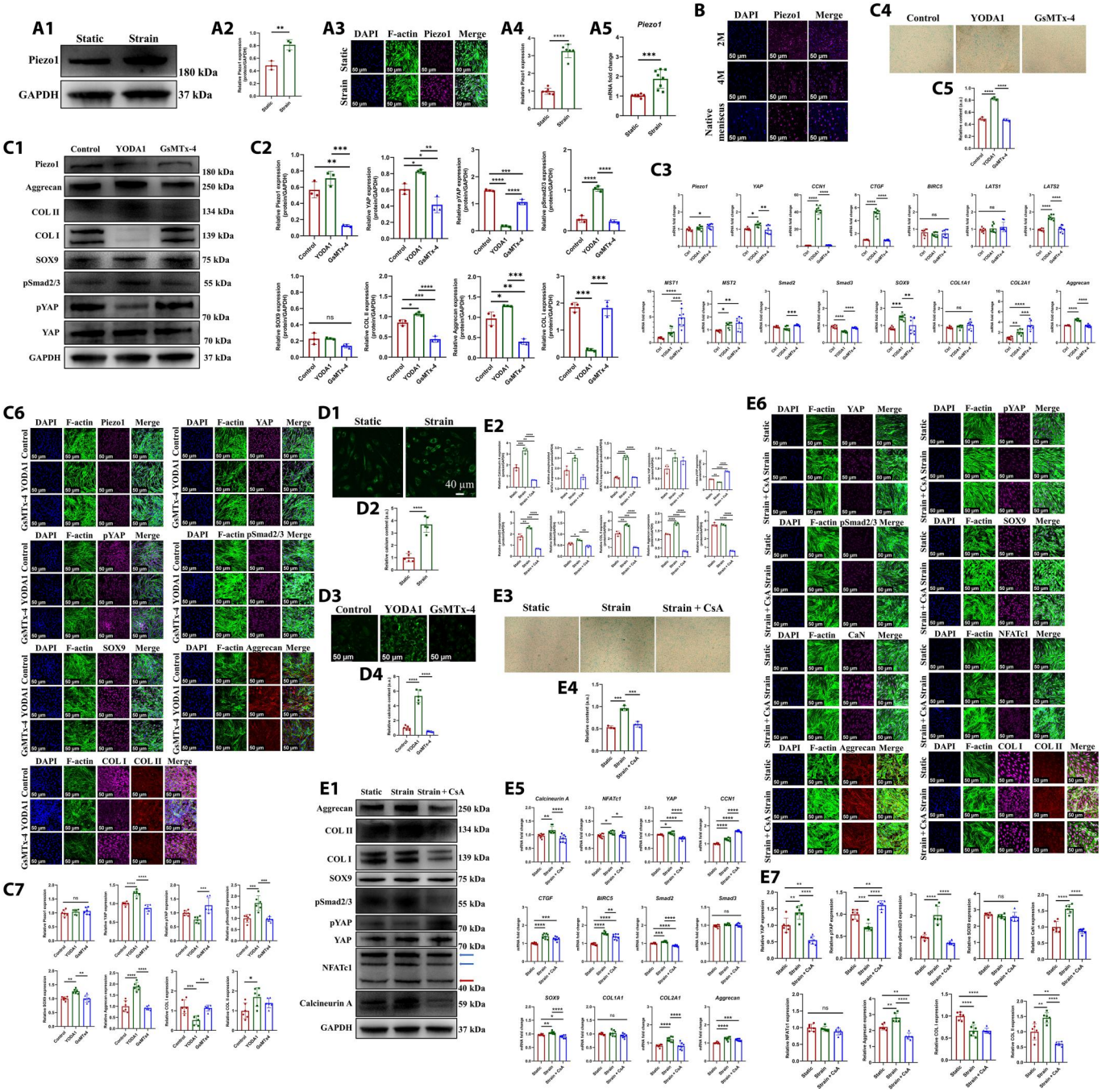

Fig. 6. Piezo1 mediates mechanotransduction on YAP-pSmad2/3-SOX9 axis through concerted activation of calcineurin and NFATc1 during MSCs chondrogenesis. (**A**) Protein and mRNA levels of Piezo1 in human SMSCs after static and CTS treatment [(A1) the Western blot analysis; (A2) the semiquantitative analysis of Western blot, $n = 3$, unpaired t test; (A3) the cell immunofluorescence; (A4) the semiquantitative analysis of cell immunofluorescence, $n = 6$, unpaired t test; (A5) the mRNA levels, $n = 8$, unpaired t test]. (**B**) Immunofluorescent assessment of Piezo1 expression in regenerated tissue of PCL scaffold + synovium transplant group and native porcine menisci. (**C**) Protein and mRNA levels in human SMSCs after being treated with YODA1 or GsMTx-4 [(C1) the Western blot analysis; (C2) the semiquantitative analysis of Western blot, $n = 3$, one-way ANOVA; (C3) the mRNA levels, $n = 8$, unpaired t test; (C4) the alcian blue staining; (C5) the semiquantitative analysis of alcian blue staining, $n = 3$, one-way ANOVA; (C6) the cell immunofluorescence; (C7) the semiquantitative analysis of cell immunofluorescence, $n = 6$, one-way ANOVA]. (**D**) Assessment of intracellular calcium content in human SMSCs [(D1) intracellular calcium content after static and CTS treatment; (D2) the semiquantitative analysis of calcium content, $n = 5$, unpaired t test; (D3) intracellular calcium content after being treated with YODA1 or GsMTx-4; (D4) the semiquantitative analysis of calcium content, $n = 5$, one-way ANOVA]. (**E**) Protein and mRNA levels in human SMSCs after CsA treatment [(E1) Western blot analysis, the red arrow represents dephosphorylated NFATc1, the blue arrows represent phosphorylated NFATc1; (E2) the semiquantitative analysis of Western blot, $n = 3$, one-way ANOVA; (E3) the alcian blue staining; (E4) the semiquantitative analysis of alcian blue staining, $n = 3$, one-way ANOVA; (E5) the mRNA levels, $n = 8$, unpaired t test; (E6) the cell immunofluorescence; (E7) the semiquantitative analysis of cell immunofluorescence, $n = 6$, one-way ANOVA]. $^{*}P < 0.05$, $^{**}P < 0.01$, $^{***}P < 0.0005$, $^{****}P < 0.0001$; ns, not significant.

(Fig. 6A). Moreover, the regenerative cells of PCL scaffold + synovium transplant group and native porcine meniscal fibrochondrocytes demonstrated robust expression of Piezo1 (Fig. 6B). Second, to identify the relation between Piezo1 and YAP-pSmad2/3-SOX9 axis, the Piezo1 agonist (YODA1) and antagonist (GsMTx-4) were applied in human SMSCs. The Piezo1 agonist up-regulated YAP expression and down-regulated pYAP content, which indicated YAP nuclear translocation. Moreover, the expression of pSmad2/3, COL II, aggrecan, and GAG was up-regulated after YODA1 treatment. However, the expression of pSmad2/3, COL II, aggrecan, and GAG was down-regulated after GsMTx-4 treatment (Fig. 6C). Thus, Piezo1 was identified as the upstream of YAP-pSmad2/3-SOX9 axis. Third, as Piezo1 was the calcium (Ca^{2+})–permeable channel, we identified whether Piezo1 regulated YAP-pSmad2/3-SOX9 axis through Ca^{2+} influx. We found that more robust Ca^{2+} influx could be observed in human SMSCs after CTS treatment (Fig. 6, D1 and D2). YODA1 treatment also led to more robust Ca^{2+} influx in human SMSCs (Fig. 6, D3 and D4). Moreover, a previous study demonstrated that Piezo1-induced Ca^{2+} influx stimulated calcineurin and then promoted concerted activation of nuclear factor of activated T c1 (NFATc1) and YAP (*33*). The calcineurin, calcium, and calmodulin-dependent heterodimeric serine/threonine phosphatase were a critical intracellular Ca^{2+} sensor (*34*). The transcription factor NFATc1 could be dephosphorylated by activated calcineurin and then translocated into nucleus, participating in multiple transcriptional activities (*35*). To determine whether Piezo1-induced Ca^{2+} influx regulated YAP-pSmad2/3-SOX9 axis through concerted activation of calcineurin and NFATc1, the antagonist of calcineurin [cyclosporin A (CsA)] and inhibitor of NFAT (VIVIT peptide) (*36*) were applied. The expression of calcineurin and dephosphorylated NFATc1 was up-regulated in human SMSCs after CTS treatment compared to those of static treatment. Subsequently, the YAP-pSmad2/3-SOX9 axis was activated. However, CsA treatment reversed the effects, demonstrating down-regulated expression of calcineurin and dephosphorylated NFATc1, followed by inhibition of YAP-pSmad2/3-SOX9 axis and down-regulation of COL I, COL II, aggrecan, and GAG (Fig. 6E). Identically, NFAT inhibitor treatment also reversed the effects of CTS, demonstrating the down-regulated expression of dephosphorylated NFATc1, followed by inhibition of YAP-pSmad2/3-SOX9 axis and down-regulation of COL II and aggrecan (fig. S23A). Next, we also evaluated the activation of calcineurin and NFATc1 in regenerated tissue and native porcine menisci. We found that the regenerative cells of PCL scaffold + synovium transplant group and native porcine meniscal fibrochondrocytes demonstrated robust expression of calcineurin A (fig. S23B) and NFATc1 (fig. S23C). Thereby, these results suggested that Piezo1 transformed biomechanics into Ca^{2+} influx followed by concerted activation of calcineurin and NFATc1, which promoted YAP-pSmad2/3-SOX9 axis during meniscal regeneration.

To further elucidate the effect of mechanics exerted by knee joint in vivo on SMSCs chondrogenesis and subsequent meniscal regeneration, the allogenic SMSCs derived from male rabbits were transplanted into meniscal defect of female rabbits. The SMSCs from male rabbits had male-specific sex-determining region Y-linked gene (SRY gene) and could be tracked using in situ hybridization (ISH) for SRY gene. At 4 weeks after operation, for SMSCs transplant group, the regenerated tissue demonstrated superior structural integrity, superficial smoothness, and bilateral marginal integration with host tissue. More cell clusters with fibrochondrocyte-like cell morphology filled the regenerated tissue. The extracellular matrix surrounding regenerative cell clusters had strongly positive Safranin O, COL I, COL II, and aggrecan expression, resembling native rabbit meniscus (fig. S24, A to D). Moreover, the colocalization of SOX9 immunofluorescence and ISH for SRY gene demonstrated robust SOX9 expression in transplanted rabbit SMSCs, indicating robust chondrogenesis (fig. S24E). However, for SMSCs transplant + condylectomy group, the regenerated tissue was inferior in defect filling, surface smoothness, and marginal integration. Only some small cells could be observed. The extracellular matrix in regenerated tissue was poor in Safranin O, COL I, COL II, and aggrecan expression (fig. S24, A to D). Moreover, the expression of SOX9 in transplanted rabbit SMSCs after condylectomy decreased significantly compared to that of SMSCs transplant group (fig. S24E). Thus, the mechanics imposed by knee joint played critical role in the chondrogenesis of SMSCs and subsequent meniscal regeneration.

The effect of matrix stiffness on YAP-pSmad2/3-SOX9 axis

As aforementioned, the mechanical property of regenerated tissue of PCL scaffold + synovium transplant group increased significantly at 4 months postoperatively compared to that of 2 months postoperatively. Previous studies demonstrated that matrix stiffness was another critical factor that affected YAP activation (*37*). Here, we hypothesized that matrix stiffness affected YAP-pSmad2/3-SOX9 axis. First, to construct different matrix stiffness condition, human SMSCs were seeded onto soft silicon rubber culture plate or traditional stiff polystyrene culture plate (Fig. 7A1). After being cultured under stiff matrix condition, the YAP-pSmad2/3-SOX9 axis was activated, demonstrating up-regulated expression of YAP, pSmad2/3, and SOX9 and down-regulated expression of pYAP. Moreover, human SMSCs demonstrated fibrochondrogenic phenotype with up-regulated expression of COL I, COL II, aggrecan, and GAG (Fig. 7, A2 to A6). Second, previous studies demonstrated that Piezo1 could sense matrix rigidity (*33*). The expression of Piezo1 was up-regulated significantly after stiff matrix treatment, followed by up-regulated expression of downstream calmodulin, calcineurin, and dephosphorylated NFATc1. Thereby, Piezo1 could sense matrix stiffness through concerted activation of calcineurin and NFATc1, followed by activation of YAP-pSmad2/3-SOX9 axis, which promoted fibrochondrogenesis of human SMSCs (Fig. 7, A2 to A6). Third, a review demonstrated that stiff substrate could promote nuclear translocation and activation of YAP through integrin-FAK (focal adhesion kinase) signaling pathway (*38*). We found that the integrin-FAK signaling was activated significantly and demonstrated up-regulated expression of integrin α5 (ITGA5), FAK, and phosphorylated FAK (pFAK). However, the phosphorylated LATS1 was down-regulated obviously, which led to reduced phosphorylation of YAP. Therefore, the stiff substrate-induced activation of integrin-FAK signaling inhibited Hippo signaling and promoted nuclear translocation and activation of YAP (Fig. 7, A2 to A6). Last, we evaluated the activation of FAK signaling in regenerated tissue of PCL scaffold + synovium transplant group and native porcine menisci. The regenerative cells and native porcine meniscal fibrochondrocytes demonstrated robust expression of FAK (Fig. 7B1) and pFAK (Fig. 7C1). The expression of FAK and pFAK in regenerative cells was up-regulated at 4 months postoperatively compared to that of 2 months postoperatively (Fig. 7, B2 and

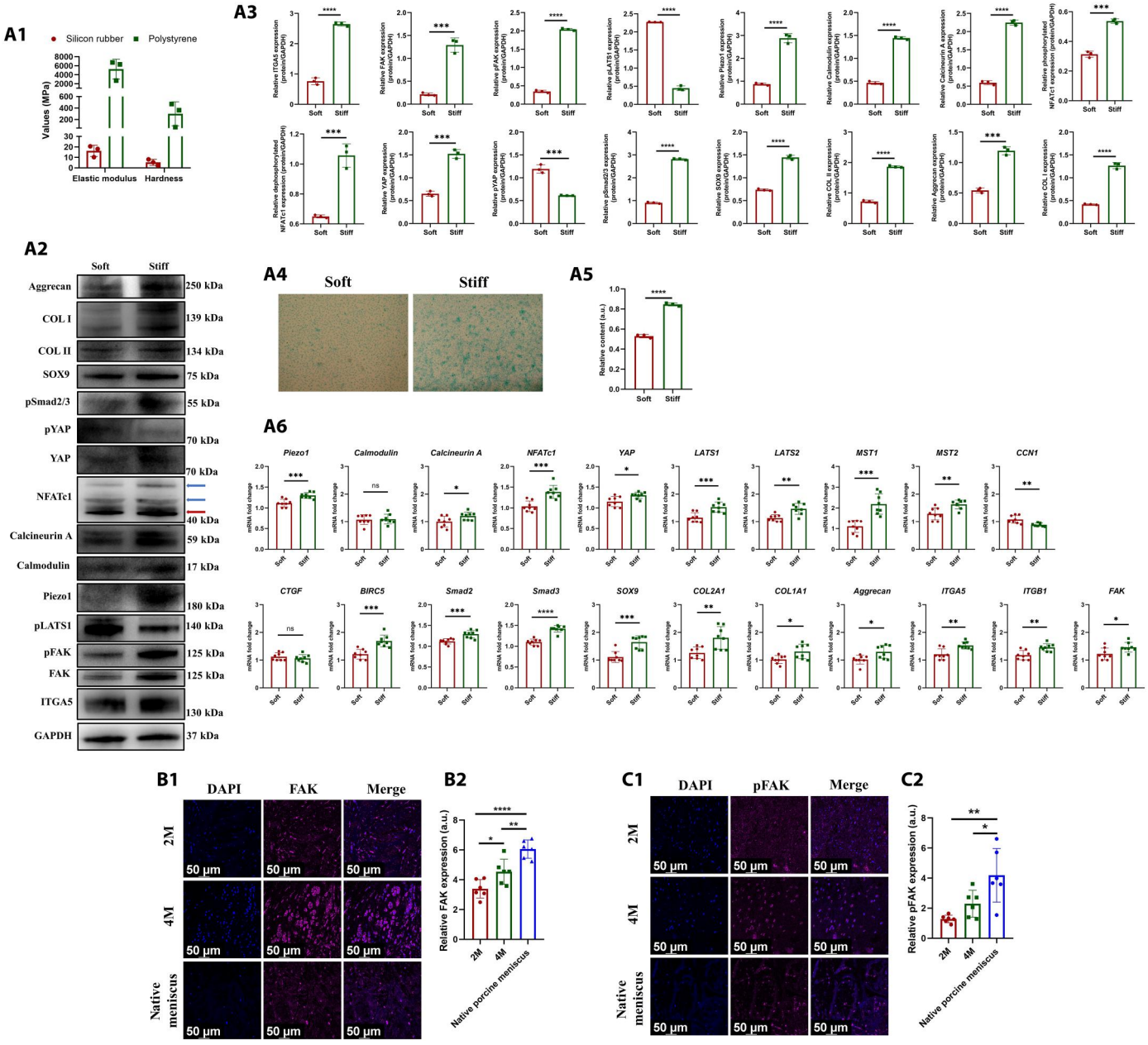

Fig. 7. The effect of matrix stiffness on YAP-pSmad2/3-SOX9 axis. (**A**) Protein and mRNA levels in human SMSCs after being treated with soft or stiff matrix [(A1) the mechanical properties of silicon rubber and polystyrene culture plate, $n = 3$; (A2) Western blot analysis, the red arrow indicates dephosphorylated NFATc1, the blue arrows indicate phosphorylated NFATc1; (A3) the semiquantitative analysis of Western blot, $n = 3$, unpaired t test; (A4) the alcian blue staining; (A5) the semiquantitative analysis of alcian blue staining, $n = 3$, unpaired t test; (A6) the mRNA levels, $n = 8$, unpaired t test]. (**B**) Immunofluorescent assessment of FAK in regenerated tissue of PCL scaffold + synovium transplant group and native porcine menisci [(B1) the immunofluorescence of FAK; (B2) the semiquantitative analysis of FAK, $n = 6$, one-way ANOVA]. (**C**) Immunofluorescent assessment of pFAK in regenerated tissue of PCL scaffold + synovium transplant group and native porcine menisci [(C1) the immunofluorescence of pFAK; (C2) the semiquantitative analysis of pFAK, $n = 6$, one-way ANOVA]. *$P < 0.05$, **$P < 0.01$, ***$P < 0.0005$, ****$P < 0.0001$; ns, not significant.

C2). Thereby, these results demonstrated that stiff matrix regulated YAP-pSmad2/3-SOX9 axis through activating Piezo1 and FAK signaling during meniscal regeneration.

Collagen cross-link remodeling during meniscal regeneration

The collagen fiber cross-link was a critical factor that determined the mechanical property of meniscus (*39*). The lysyl oxidase (LOX) and lysyl hydroxylase (LH) are the main enzymes that catalyze collagen cross-linking (*40*, *41*). A previous study demonstrated that Piezo1 led to up-regulation of collagen cross-linking enzyme-

LOX in native tendon tissue (*42*). Here, we hypothesized that Piezo1 channel was the upstream of collagen cross-linking enzyme during meniscal regeneration. As aforementioned, we found that Piezo1 was up-regulated in human SMSCs after CTS or stiff matrix treatment. First, we found that the expression of LOX and LH2 (a member of LH family) was up-regulated significantly in human SMSCs after CTS treatment. The mRNA of LOX, LH1, LH2, and LH3 were all up-regulated (Fig. 8A). In addition, the expression of LOX and LH in human SMSCs was up-regulated after Piezo1 agonist-YODA1 treatment but was down-regulated after Piezo1 antagonist–GsMTx-4 treatment (Fig. 8B). Besides, stiff matrix up-regulated the expression of LOX and LH in human SMSCs (Fig. 8C). Second, we evaluated the expression of LOX and LH2 in regenerated tissue of PCL scaffold + synovium transplant group and native porcine menisci. The regenerated tissue and native porcine menisci demonstrated robust expression of LOX (Fig. 8D) and LH2 (Fig. 8E). Thereby, the biomechanics and stiff matrix–induced up-regulation of Piezo1 facilitated expression of LOX and LH, which catalyzed collagen cross-link during meniscal regeneration.

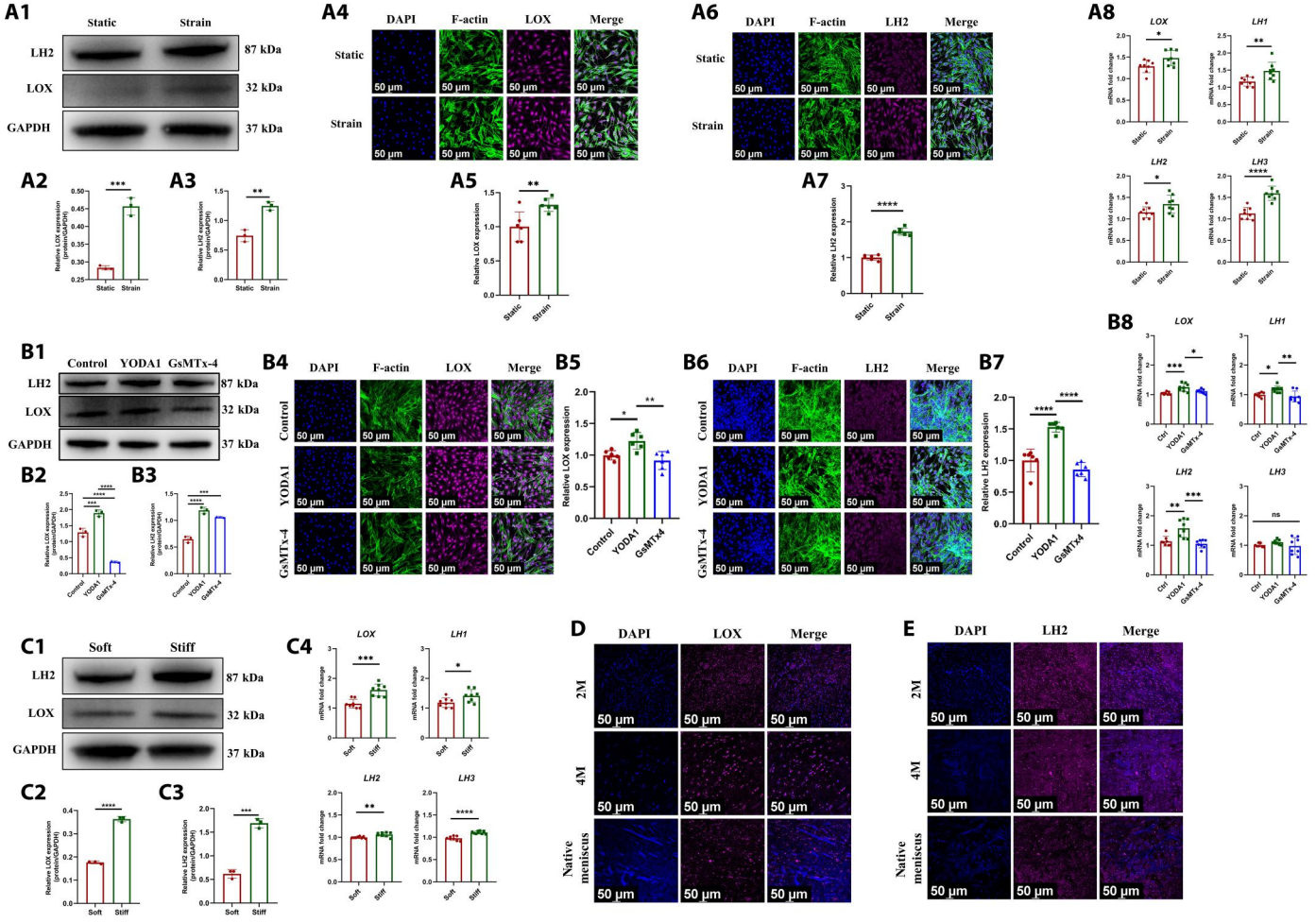

Fig. 8. The biomechanical stimulus and matrix stiffness regulate the expression of collagen cross-link enzymes (LOX and LH) through Piezo1. (**A**) Protein and mRNA levels of LOX and LH in human SMSCs after static or CTS treatment [(A1) the Western blot analysis; (A2) the semiquantitative analysis of LOX, $n = 3$, unpaired t test; (A3) the semiquantitative analysis of LH2, $n = 3$, unpaired t test; (A4) the cell immunofluorescence of LOX; (A5) the semiquantitative analysis of LOX immunofluorescence, $n = 6$, unpaired t test; (A6) the cell immunofluorescence of LH2; (A7) the semiquantitative analysis of LH2 immunofluorescence, $n = 6$, unpaired t test; (A8) the mRNA levels, $n = 8$, unpaired t test]. (**B**) Protein and mRNA levels of LOX and LH in human SMSCs after being treated with YODA1 or GsMTx-4 [(B1) the Western blot analysis; (B2) the semiquantitative analysis of LOX, $n = 3$, one-way ANOVA; (B3) the semiquantitative analysis of LH2, $n = 3$, one-way ANOVA; (B4) the cell immunofluorescence of LOX; (B5) the semiquantitative analysis of LOX immunofluorescence, $n = 6$, one-way ANOVA; (B6) the cell immunofluorescence of LH2; (B7) the semiquantitative analysis of LH2 immunofluorescence, $n = 6$, one-way ANOVA; (B8) the mRNA levels, $n = 8$, one-way ANOVA]. (**C**) Protein and mRNA levels of LOX and LH in human SMSCs after being treated with soft or stiff matrix [(C1) the Western blot analysis; (C2) the semiquantitative analysis of LOX, $n = 3$, unpaired t test; (C3) the semiquantitative analysis of LH2, $n = 3$, unpaired t test; (C4) the mRNA levels, $n = 8$, unpaired t test]. (**D**) Immunofluorescent assessment of LOX expression in regenerated tissue of PCL scaffold + synovium transplant group and native porcine menisci. (**E**) Immunofluorescent assessment of LH2 expression in regenerated tissue of PCL scaffold + synovium transplant group and native porcine menisci. $^*P < 0.05$, $^{**}P < 0.01$, $^{***}P < 0.0005$, $^{****}P < 0.0001$; ns, not significant.

DISCUSSION

Here, we identified that MSCs participated in maturation and regeneration of meniscus using MSC-tracing transgenic mice model. The present study demonstrated that the synovial tissue contained abundant intrinsic MSCs, which had superior chondrogenic capacity, and growth factors, including TGFβ1 and CTGF. We developed an effective and translational strategy to facilitate meniscal regeneration using 3D printing biomimetic meniscal scaffold combining autologous synovium transplant, which was distinct from traditional tissue engineering strategy using exogenous growth factors or cell transplantations. We concluded that this facilitated anisotropic meniscus–like tissue regeneration and protected cartilage from degeneration in porcine subtotal meniscectomy model. Mechanistically, the biomechanics and matrix stiffness up-regulated Piezo1 expression in MSCs, facilitating concerted activation of calcineurin and NFATc1, further activated YAP-pSmad2/3-SOX9 axis, and consequently facilitated fibrochondrogenesis of MSCs during meniscal regeneration. In addition, Piezo1 induced by biomechanics and matrix stiffness up-regulated collagen cross-link enzyme expression in MSCs, which catalyzed collagen cross-link and thereby enhanced mechanical properties of regenerated tissue.

3D printing PCL scaffold combining autologous synovium transplant facilitated regeneration of anisotropic meniscus–like tissue and alleviated cartilage degeneration in porcine subtotal meniscectomy model. The neomenisci demonstrated anisotropic distribution of matrix. The inner and middle zones were rich in COL II, aggrecan, and GAG, whereas the outer zone mainly contained COL I. Previous study demonstrated that the COL II, aggrecan, and GAG matrix mainly held the capacity to resist compression, while the COL I content mainly resist tension (*9*). Thus, the anisotropic distribution of matrix in the regenerated tissue could absorb shock exerted by knee joint motion like native menisci. The shock absorption function of regenerated tissue was beneficial to restore the mechanical homeostasis of knee joint, which could protect joint hyaline cartilage from degeneration, demonstrating less cartilage abrasion and lower OARSI scores. The meniscus was a typical weight-bearing tissue, leading to excessive mechanics on meniscal cells (*26*). To maintain mechanical homeostasis, the meniscal fibrochondrocytes were surrounded by a narrow tissue region called PCM. The PCM together with the enclosed chondrocyte was termed as the "chondron" (*43*). Previous studies have suggested that PCM played a critical role in controlling mechanical microenvironment and mechanobiology of chondrocytes or fibrochondrocytes (*26*, *44*). In the present study, the regenerative cells contained abundant perlecan and COL VI, the main PCM of fibrochondrocytes, which may be responsible for mechanotransduction of regenerative cells. In addition, by means of angiography, we observed that the regenerated tissue contained abundant blood vessels, indicating good blood supply relationship between regenerated tissue and perimeniscal tissue. In addition, blood supply could provide necessary nourishment for meniscal regeneration (*45*). However, the quantities of blood vessels decreased as the maturity of regenerated tissue, like the maturation of native human menisci, demonstrating that only peripheral 10 to 25% remained vascularized in adult (*1*). Previous studies demonstrated that aggrecan and GAG inhibited the adhesion and migration of blood vessel endothelial cells in a dose-dependent manner (*46*, *47*). Thereby, the remodeling of angiogenesis in regenerated tissue could be attributed to the increased deposition of aggrecan and GAG in the inner and middle zones. In all, the anisotropic meniscus–like tissue was obtained using 3D printing scaffold implant combining autologous synovium transplant.

The biomechanical and biochemical stimuli and matrix stiffness played critical roles in meniscal regeneration. A previous study constructed the anisotropic-engineered meniscus in vitro using orchestrated biomechanical and biochemical stimuli (*9*), further clarifying the synergistic effects of these two stimuli in meniscal regeneration. In the present study, knee joint compression could provide optimal biomechanical stimulus for meniscal regeneration. TGFβ and CTGF growth factors within native synovium could provide biochemical stimulus. We also identified the synergistic effect of TGFβ and CTGF on inducing fibrochondrogenic differentiation of SMSCs. The RNA-seq analyses demonstrated that TGFβ signaling and Hippo signaling were enriched in regenerated tissue. The TGFβ signaling played a critical role in chondrogenesis and the maintenance of chondrogenic phenotype (*48*). However, in native cartilage, TGFβ usually appeared as the complex of TGFβ–latent TGFβ–binding protein, thus inhibiting its activity. TGFβ could be released from the complex after mechanical stress and then activated TGFβ signaling (*49*). In the present study, we speculated that the biomechanical stimulus caused by joint compression released and activated TGFβ, which could be reflected by the robust expression of downstream pSmad2/3 in regenerated tissue. YAP is the critical effector of Hippo signaling. Previous studies demonstrated that YAP activity could be regulated by mechanics and matrix stiffness and controlled cell fate (*38*). We found that YAP was up-regulated and translocated into the nucleus as maturity of regenerated tissue. Previous study demonstrated that YAP dictated the localization of Smad2/3 by forming YAP-Smad2/3 complexes, namely, Smad2/3 could be sequestered in the nucleus as YAP is translocated into the nucleus (*29*). In addition, Smad3 could enhance SOX9-dependent transcriptional activation in primary chondrogenesis by forming Smad3/SOX9 complex (*30*, *50*). Last, we identified that the biomechanics-induced YAP-pSmad2/3-SOX9 axis facilitated chondrogenesis of SMSCs and subsequent meniscal regeneration. The mechanosensitive ion channel Piezo1 played a critical role in musculoskeletal system, which could relay the biomechanical stimulus into chemical signals (*42*, *51*, *52*). In the present study, it was demonstrated that Piezo1 mediated mechanotransduction through concerted activation of calcineurin and NFATc1 and further activated YAP-pSmad2/3-SOX9 axis during meniscal regeneration. Furthermore, previous studies demonstrated that YAP activity could be regulated by FAK signaling activated by stiff matrix. The focal adhesion signaling driven by FAK could be activated by integrin engagement in the stiff matrix microenvironment. The Hippo pathway and YAP activity could be modulated by FAK in various ways (*38*). A previous study concluded that stiff matrix could evoke the ITGA5-FAK axis in fibroblasts (*53*). We identified that the ITGA5-FAK axis was also activated in SMSCs when seeded onto stiff substrate, further inhibiting Hippo signaling and phosphorylation of YAP. In addition, we found that the activity of FAK signaling increased as maturity of regenerated tissue, which corresponded to its increased mechanical property. Thereby, the increased mechanical properties of regenerated tissue contributed to the maturity and maintenance of fibrochondrogenic phenotype of regenerative cells by modulating YAP activity through FAK signaling. The mechanosensitive ion channel, Piezo1, not only relayed

biomechanical stimulus into chemical signals but also mediated the effects of matrix stiffness (*54*). Here, we clarified that Piezo1 could sense matrix stiffness through concerted activation of calcineurin and NFATc1, followed by activation of YAP-pSmad2/3-SOX9 axis, which promoted fibrochondrogenesis of SMSCs.

The biomechanical stimulus and stiff matrix–induced Piezo1 activation up-regulated the expression of LOX and LH in MSCs, which facilitated collagen cross-link in regenerated tissue. In native meniscus, the collagen fibers were not independent; at the nanoscale, adjacent collagen fibers shared several individual collagen fibrils and were interconnected by these fibrils (*55*). Moreover, the collagen fibrils were cross-linked by the catalysis of LOX and LH (*56*). This closely intertwined and cross-linked structure enabled the menisci to sustain complex compressive, tensile, and shear stress (*55*). A previous study clarified that Piezo1-induced Ca^{2+} influx led to up-regulation of collagen cross-linking enzyme-LOX in native tendon tissue (*42*). We found that the expression of LOX and LH was up-regulated in SMSCs after being treated with CTS, YODA1, or stiff matrix. It was speculated that the Piezo1-induced Ca^{2+} influx contributed to up-regulation of LOX and LH during meniscal regeneration; however, the exact mechanisms needed to be further clarified. Moreover, the collagen fiber arrangement reflected by Sirius red resembled that of native menisci as the maturity of regenerated tissue. Thereby, the up-regulation of LOX and LH induced by biomechanical stimulus and stiff matrix played a critical role in collagen cross-link remodeling and thus enhanced mechanical properties during meniscal regeneration. The molecular mechanism of MSCs′ chondrogenesis and collagen cross-link remodeling stimulated by biomechanical, biochemical, and stiff matrix factors was illustrated in fig. S25.

Some limitations still existed in the present study: (i) We could not label SMSCs directly using transgenic model due to the absence of specific markers for SMSCs. (ii) We mainly observed the molecular function of mechanosensitive factors (Piezo1 and YAP); however, other mechanosensitive or nonmechanosensitive factors may also play critical roles in meniscal regeneration. (iii) We mainly clarified the functions and mechanisms of SMSCs in facilitating meniscal regeneration, whereas other cell types, such as immune cells or fibroblasts within synovium, may also participate in meniscal regeneration. (iv) The experiment was only followed up for 4 months; thereby, long-term effects of meniscal regeneration and remodeling as well as chondroprotection was not be evaluated. (v) The biochemistry and enzyme-linked immunosorbent assay were not performed to measure the content of collagen and GAG.

In conclusion, we clarified that MSCs participated in meniscal maturation and regeneration using MSCs tracing transgenic mice model. In addition, 3D printing PCL scaffold combining autologous synovium transplant facilitated the regeneration of anisotropic meniscus–like tissue and protected cartilage from degeneration in large animal model. Mechanistically, the biomechanics and matrix stiffness up-regulated Piezo1 expression in MSCs, facilitating calcium influx and concerted activation of calcineurin and NFATc1, and further activated YAP-pSmad2/3-SOX9 axis during meniscal regeneration. Furthermore, Piezo1 induced by biomechanics and matrix stiffness up-regulated LOX and LH expression in MSCs, which catalyzed collagen cross-link and thereby enhanced mechanical properties of regenerated tissue. Thus, 3D printing biomimetic meniscal scaffold combining autologous synovium transplant would be an effective and translational strategy to regenerate meniscal fibrocartilage in the future, which warranted further investigation in clinic. The schematics diagram of 3D-printed PCL scaffold implant combining autologous synovium transplant on facilitating meniscal fibrocartilage regeneration was illustrated in fig. S26.

MATERIALS AND METHODS

Construction of native meniscal 3D model

2D images of medial meniscus from a male minipig cadaver (age, 12 months; weight, 40 kg) were obtained by micro–computed tomography (micro-CT) scanning (GE Healthcare, USA). The 2D files were imported into Mimics software (version 19.0, Materialise, Belgium). The following steps were performed to finish the segmentation of meniscal tissue and construction of meniscal 3D model: (i) using the function of "multiple slice edit" and "thresholding" to separate meniscal tissue and (ii) using the function of "Region Growing" to establish a meniscus "Mask." After selecting this function, all the internal tissues of the meniscus could be selected after clicking on the tissues of the meniscus, while the tissues outside the meniscus were removed. (iii) After the establishment of Mask, a 3D meniscal model could be constructed using "Calculating 3D function," and then, the sterelithography (STL) format can be exported. (iv) The meniscal 3D model was then imported into Geomagic software (Geomagic Wrap 2015, USA), the spikes on the surface were removed, and the triangular surface was optimized to further optimize the surface quality of the model. The STL format file was then exported. In addition, the 3D models of human, rabbit, and beagle canine menisci were constructed identically.

Construction of meniscal printing model, supporting printing structure and printing path design

The 3D model of native meniscus was imported into 3D bioprinter (3D-Bioplotter, EnvisionTEC, Germany), which was equipped with processing software (Perfactory RP). The 3D-Bioplotter was an XYZ robotic arm apparatus (*57*). The material was extruded, driven by the pneumatic pressure of nitrogen. The following steps were performed to finish the printing design: (i) Uniform slicing for main subject: A nozzle with inner diameter of 400 μm was selected for PCL [weight-average molecular weight (*M*w), 43 to 50 kDa; 19561-500, Polysciences, USA] extrusion. Considering mild collapse of melted PCL before solidification, the slicing thickness of each layer was set as 80% of inner diameter of the nozzle, i.e., 320 μm. (ii) Using the function of "Support Generation for Bioplotter," a supporting structure could be designed to fill in the blank space between suspended part of meniscal bottom and printing platform. Here, the optimal parameters of supporting model were set as: polygon offset (600 μm), layer thickness (320 μm), and detail threshold (800 μm). The polygon offset (600 μm) means that the edge of the supporting model was 600-μm wider than the boundary of the main subject. The layer thickness (320 μm) means that the slicing thickness of each layer was 320 μm. The detail threshold (800 μm) means that supporting printing was performed if the vertical distance between meniscal bottom and printing platform exceeded 800 μm. Because of the superiority of Pluronic F-127 (P2443, Sigma-Aldrich, USA) in rheological property, water solubility, printability, and viscidity, it is an ideal sacrificial material for supporting printing. Therefore, a nonionic surfactant Pluronic F-127 was selected for the printing of supporting structure, which

had good printability and good adherence to PCL material, and it could be easily removed by water. For the main subject printing, the printing path design includes inner printing structure and contour. The printing path was designed according to native collagen fiber orientation, demonstrating circumferential and radial arrangement. The construction of meniscal printing model, supporting printing structure and printing path design, was identical for porcine, rabbit, human, and beagle canine meniscal scaffold.

To construct meniscal model with flat bottom, native porcine meniscal 3D model was imported into 3D processing software (Freeform, USA). The bottom was trimmed flat and then exported into STL format file. The subsequent uniform slicing was completed identical to native meniscal model.

Preparation of printing materials and identification of printing conditions

A total of 30% (w/v) Pluronic F-127 solution was prepared for the printing of supporting structure. Briefly, 9 g of Pluronic F-127 powder was immersed into 30 ml of deionized water and then maintained at 4°C to ensure dissolution. After complete dissolution, centrifugation (1000 rpm, 5 min) was required to remove bubbles. Then, the Pluronic F-127 solution was injected into the low-temperature material barrel through a bypass. Before printing, the solution was maintained at 25°C for at least 20 min to reduce its mobility. PCL pellets were put into high-temperature material barrel. The barrel temperature was set as 150°C. Before printing, PCL material was heated for at least 10 min to ensure material melting, and then, the temperature was maintained throughout the whole printing process.

Afterward, the optimal printing parameters for each material were identified. In this stage, a simple printing model (10 mm by 10 mm by 1 mm) was designed. This model was also used for subsequent cell seeding and cytocompatibility assessment of PCL scaffold in vitro. The standard for optimal printing parameters included optimal extrudability and consistent printing strands. Moreover, the width of printing strand was consistent with the designed width. After meeting the aforementioned conditions, the optimal printing parameters could be confirmed.

Shore hardness testing of native porcine meniscus and PCL

For native porcine menisci, three porcine medial menisci were harvested from fresh knee specimen. The menisci were wrapped with gauze soaked with 0.9% sodium chloride solution. Then, the menisci were bisected into femoral and tibial aspects from the axial plane and were further divided into anterior, central body, and posterior segments. For PCL shore hardness testing, PCL materials of two commonly used molecular weights (43 to 50 kDa and 80 kDa) were selected for hardness testing. Three standard dumbbell-shaped samples (10 cm by 2 cm by 2 mm) of each PCL material were prepared for hardness testing.

During testing, the meniscus specimen was attached to the sample holder with cyanoacrylate cement. The sample holder was fixed with a flexible spherical joint and lead screw assembly to allow the test surface perpendicular to the loading shaft. Then, a spherical indenter was applied to the test surface until the equilibrium between compression force and counterforce was reached. Measurements were taken at regular intervals of 5 mm apart. Three measurements were taken for each sample, and then, the mean value was calculated. For PCL testing, the PCL sample was placed in the sample holder, and then, identical operation was performed to finish hardness testing. The measurements were performed according to a previous study (*58*).

Scanning electrical microscopy

The scaffold surface topography and strand arrangement were assessed by scanning electrical microscopy (SEM; JSM-7900F, Japan). Three supporting printing meniscal scaffolds were prepared. One intact scaffold was used to assess the femoral aspect. Another one intact scaffold was applied to observe the tibial aspect. The last one scaffold was divided into anterior, central body, and posterior segments, which were used to assess the cross section. Last, the samples were sputter-coated with gold and visualized using SEM at 3.0 kV.

The characterization of tibial plateau

After removing distal bone segment and extra soft tissues, the medial tibial plateau of porcine was exposed. Then, the photographs of tibial plateau from top, anterior, posterior, and medial views were taken. After removing all soft tissues, the tibial plateau was scanned by micro-CT scanner (GE Healthcare, USA). The 2D files were imported into Mimics software (version 19.0, Materialise, Belgium). Using the function of "bone segmentation," the bone division and construction of tibial plateau 3D model were finished later. The screenshots of tibial plateau 3D model from top, anterior, posterior, and medial views were also taken. For quantitative analysis of medial tibial plateau morphology, four points (medial intercondylar notch, anterior rim, medial rim, and posterior rim) were selected in the medial tibial plateau. Then, the vertical distances among points were measured. The tibial plateau of other species (goat, canine, and rabbit) was obtained and characterized with identical methods. The 2D files of human knee were acquired from a patient who was performed with CT scanning.

The compatibility between meniscal scaffold and tibial plateau in vitro

To assess the matching property between scaffold and tibial plateau, the supporting-printing or flat-printing scaffolds were prepared for subsequent transplantation. Several nonabsorbable 2-0 Ethibond sutures were threaded across meniscal scaffold for subsequent fixation. After removing medial meniscus, the scaffold was implanted anatomically, followed by fixation to the surrounding soft tissue with sutures. Then, photographs from anterior, posterior, medial, and top views were taken to assess the compatibility between scaffold and tibial plateau.

Finite element analysis of load distribution in meniscus and tibial plateau

For porcine knee joint, as aforementioned, the proximal tibial plateau and medial meniscus specimens were scanned by micro-CT scanner (GE Healthcare, USA). For human knee joint, the knee magnetic resonance imaging data of a volunteer were obtained by a 1.5-T scanner (Signa, GE Healthcare, Waukesha, Wisconsin, USA) with a 3.5-mm slice spacing and 512 × 512 matrix using our standard knee magnetic resonance protocol providing assessment in three planes. All procedures performed in studies involving human participants were in accordance with the ethical standards of the institutional and/or national research committee and with the 1964 Helsinki Declaration and its later amendments or comparable

ethical standards. The 3D reconstruction of bone structure and soft tissues was completed by using MIMICS 19.0 (Materialise, Leuven, Belgium).

The 3D models were exported as STL files and imported into Geomagic Studio software (version 12.0, Geomagic Inc., Morrisville, NC, USA) for smoothing for further finite element modeling. The models were exported as IGES files and imported in ANSYS 17 (ANSYS, Houston, TX, USA). The material properties of bone and meniscus were identified according to a previous study (*59*). In particular, the material property of bone was linear with an elastic modulus (E) of 17 GPa and a Poisson′s ratio (ν) of 0.3. The elasticity modulus and Poisson′s ratio of the meniscus were 3 MPa and 0.46, respectively. Simulating static stance, a perpendicular compressive stress of 400 N was applied on the medial compartment of human tibial plateau. For porcine knee, a vertical compression of 125 N was applied on the medial compartment of tibial plateau. The distal side of the tibia was fixed. The anterior horn, posterior horn, and middle medial side of the meniscus were fixed on the tibial plateau. The contact between the meniscus and tibia plateau were set as frictionless condition. The distribution of compression on the medial menisci and medial tibial plateau was analyzed.

Mice model

All animal experiments were approved by the animal experimental ethics committee of Peking University. All applicable institutional and/or national guidelines for the care and use of animals were followed. Ten *Pdgfrα-CreER*; *Rosa26-LSL-Tdtomato* transgenic mice were prepared. The intraperitoneal injection of tamoxifen was started at 8 weeks after birth once a day for 1 week. Two mice were executed at 10 weeks after birth. The menisci were assessed with immunofluorescent costaining, including RFP/COL I/COL II, RFP/SOX9, PDGFRα/COL I/COL II, and PDGFRα/SOX9. Another four mice (eight knees) were performed with meniscectomy in medial menisci. The total meniscectomy or partial meniscectomy of anterior half part of medial meniscus was prepared. Each group contained four knees. All knees were harvested at 3 months postoperatively. The menisci were embedded with paraffin and sectioned continuously. Meniscal regeneration was assessed by immunofluorescence and histology.

Rabbit model

To evaluate the effect of mechanics on SMSCs chondrogenesis during meniscal regeneration, the condylectomy of MFC was performed after allogenic rabbit SMSCs were transplanted into meniscal defect. A total of eight adult rabbits (female, 6 months, 2.5 ± 0.5 kg) were used. The SMSCs transplant group and SMSCs transplant + condylectomy group were included. First, a cylindrical full-thickness defect with a diameter of 2.0 mm was prepared with corneal trephine in the avascular portion of anterior horn of medial meniscus in the right knee according to a previous study (*16*). The left knees served as native group. To track the fate of transplanted SMSCs, SMSCs from male rabbits (male, 6 months, 2.5 kg) were transplanted into female rabbits. The transplanted male SMSCs could be distinguished from host cells by ISH for male-specific SRY gene. For SMSCs transplant group, a total of 1×10^4 SMSCs encapsulated with 5% methacrylated gelalin (gel-MA) [containing 1% phenyl (2,4,6-trimethylbenzoyl) phosphinic acid lithium salt (LAP) photoinitiator] solution was injected into a mold (2 mm in diameter, 1 mm in depth). The gel-MA solution was cured by blue light for 10 s and then transplanted into meniscal defect. For SMSCs transplant + condylectomy group, after SMSCs transplantation, the MFC was removed. The samples were collected for histological analyses at 4 weeks after operation.

Porcine model

Nineteen adult minipigs (female, 1 year, 50 ± 5 kg) were included. The detailed group information was described in table S3. The PCL scaffold + synovium transplant group, blank PCL scaffold group, subtotal meniscectomy group, and sham group were included. The standard anesthesia, skin preparation, and disinfection were performed according to a previous study (*60*). The standard medial parapatellar approach (*61*) was used to expose joint cavity, and then the patella was dislocated laterally. To fully expose medial meniscus, the rectangular bone block of medial collateral ligament upper attachment site in MFC was removed using oscillating saw. The tibia was rotated externally to fully expose medial meniscus. Subtotal meniscectomy (90% excision) was performed in medial meniscus with the peripheral 10% meniscal tissue remaining. In PCL scaffold + synovium transplant group, the 3D printing PCL scaffold was fixed with the residual meniscal tissue using 2-0 Ethibond sutures. Afterward, the synovial tissue was harvested from suprapatellar bursa and spread on the PCL scaffold. Then, the tibia was rotated internally to ensure that the synovial tissue was immobilized between MFC and scaffold. The bone block of medial collateral ligament was fixed anatomically with nails. Last, the incision was closed layer by layer using sutures. In blank PCL scaffold group, only the PCL scaffold was implanted. In subtotal meniscectomy group, only subtotal meniscectomy was performed. In sham group, no meniscectomy was performed, and the remaining procedures were identical to meniscectomy group. After the operation, minipigs were restricted in small cages (1.2 m × 1.2 m × 1.2 m) to avoid unexpected trauma. The nonsteroidal anti-inflammatory drugs and penicillin were administered intramuscularly for 2 weeks. Then, minipig was allowed to move freely in large pigpens (3 m × 3 m × 3 m).

Arthroscopic assessment

Arthroscopic examination was performed using the arthroscope (Smith Nephew, USA). Standard skin preparation and disinfection in knee joint were performed. After touching the patella, patellar tendon, and joint space, the contour of knee joint was identified. The standard anteromedial portal was used for preliminary detection. An incision of 5 mm in length was made in the medial side adjacent to patellar tendon. A trochar was introduced through the anteromedial portal, and then the arthroscope was introduced into the joint cavity through the trochar. The meniscal regeneration and cartilage status were examined arthroscopically. Last, the portals were closed using 2-0 suture (Ethicon, USA).

Angiography and blood vessel 3D reconstruction

The angiography was performed using the angiographic contrast agent (Microfil, MV-122, Flow Tech Inc., USA). The femoral artery was separated, followed by puncture using a 16-gauge needle. Then, the angiographic contrast agent was injected. The regenerated meniscal tissue or native porcine menisci were harvested and then scanned with micro-CT. Last, the 2D files were imported into Mimics software (version 19.0, Materialise, Belgium) to reconstruct 3D model of blood vessels.

Cell isolation and expansion

After Institutional Review Board approval, human synovial tissue was harvested from suprapatellar bursa during an arthroscopic operation that was doing meniscectomy or meniscal repair. The synovium was minced and digested with 0.4% type I collagenase (Gibco, USA) for 4 hours at 37°C. The resultant mixture was filtered with 70-μm nylon filter to remove undigested debris. Cells were washed with phosphate-buffered saline (PBS), centrifuged twice, and then resuspended with α–minimum essential medium (α-MEM) containing 10% fetal bovine serum (FBS), penicillin (100 U/ml), and streptomycin (100 mg/ml) (Invitrogen, USA). The resuspended cells were cultured in Φ 10-cm culture dishes. Cells were allowed for attachment for 2 days, and nonadherent cells were removed through changing medium every 2 days. After 14 days, cells were digested with trypsin-EDTA (0.25% trypsin and 1 mM EDTA; Hyclone, USA) and regarded as passage 0 (P0). Then, the P0 SMSCs were passaged at a ratio of 1:3. Subsequent passage was performed when the confluence reached 80 to 90%. The SMSCs at P2 were used for subsequent experiments. For the isolation and expansion of male rabbit SMSCs, the synovial tissue was harvested from suprapatellar bursa. The subsequent procedures were identical to the isolation and expansion of human SMSCs.

Cell treatment

To evaluate the effect of mechanical strain on human SMSCs phenotypes in vitro, the CTS was applied using the train culture system (Flexcell, FX5K Tension, USA). Human SMSCs were seeded onto the matched six-well culture plate coated with collagen type I (Flexcell, BF-3001C) at a density of 15,000 cells/cm^2. SMSCs were incubated for 24 hours in 10% FBS-supplemented α-MEM, following 12 hours of culture in serum-free α-MEM before CTS. To simulate physiological condition in native menisci, the parameters of uniaxial CTS were set as 5% strain with stretching frequency of 0.5 Hz (*28*, *50*). The unstretched human SMSCs seeded on the same culture plate were used as controls. The protein and mRNA were collected immediately after stretching for 4 hours. To induce phosphorylation and cytosolic translocation of YAP, human SMSCs were treated with 10 μM dihydrexidine hydrochloride (HY-101299B, MCE) for 4 hours. To inhibit phosphorylation of Smad3, human SMSCs were treated with 5 μM SIS3 HCL (S7959, Selleck) for 4 hours. To activate Piezo1, human SMSCs were treated with 50 μM YODA1 (HY-18723, MCE) for 4 hours. To suppress Piezo1, human SMSCs were treated with 2 μM GsMTx-4 (HY-P1410, MCE) for 4 hours. To suppress calcineurin, human SMSCs were treated with CsA (0.1 μg/ml; HY-B0579, MCE) for 4 hours. To suppress NFATc1, human SMSCs were treated with 10 μM NFAT inhibitor (VIVIT peptide, HY-P1026, MCE) for 4 hours. To evaluate the effect of substrate rigidity on human SMSCs phenotypes, the traditional polystyrene culture plate was used as stiff matrix, while the silicon rubber culture plate (Flexcell, BF-3001C) was used as soft matrix. Human SMSCs were cultured in soft or stiff substrate for 4 hours.

Human SMSCs seeding onto PCL scaffold and growth factor treatment

As mentioned above, a simple printing model (10 mm by 10 mm by 1 mm) was used to seed cells. PCL scaffolds were disinfected by 75% ethanol for 2 hours and then washed with PBS. The sterile bottle caps of 15-ml centrifuge tubes were settled in the six-well culture plate. One disinfected scaffold was placed in one cap. Human SMSCs suspension was added to the bottle cap (1×10^6 cells per cap). After 4 hours, the supernatant in the bottle cap was aspirated to remove nonadherent cells. After culturing for 3 days, the live-dead staining (calcein-AM and propidium iodide kit, Invitrogen, USA) and cytoskeleton staining (Alexa Fluor 488 phalloidin kit, A12379, Thermo Fisher Scientific, USA) were performed to assess the cytocompatibility of PCL scaffold. In addition, human SMSCs were treated with α-MEM, α-MEM + TGFβ1 (10 ng/ml) (100-21, PeproTech, USA), α-MEM + CTGF (100 ng/ml) (120-19, PeproTech, USA), and α-MEM + TGFβ1 (10 ng/ml) + CTGF (100 ng/ml) for 7 or 14 days. Afterward, the crystal violet staining (G1062, Solarbio, China) was used to assess proliferation, alcian staining (G1562, Solarbio, China) was used to assess GAG production, and cell immunofluorescence was used to assess the expression of COL I, COL II, and SOX9. The ImageJ software was used for subsequent semiquantitative analysis of cell proliferation, GAG, COL I, COL II, and SOX9.

Western blot

Total proteins were extracted from human SMSCs using radioimmunoprecipitation assay lysis buffer (C1053, Applygen, China) containing protease inhibitor (P1265-1, Applygen, China) and phosphatase inhibitor (P1260-1, Applygen, China). The protein concentrations were determined by using NanoDrop (Thermo Fisher Scientific, USA) at 280-nm ultraviolet. The proteins were separated on 4 to 20% bis-tris polyacrylamide gel (M00930, GenScript, China) electrophoresis and then transferred onto polyvinylidene fluoride (PVDF) membranes (ISEQ00010, Millipore, USA) according to standard procedures. The PVDF membranes were blocked with 5% (w/v) bovine serum albumin (BSA) (P1621, Applygen, China) for 1 hour at room temperature. The membranes were incubated with corresponding primary antibodies overnight at 4°C. Subsequently, the corresponding secondary antibodies were incubated for 1 hour at room temperature. The enhanced chemiluminescence ultra western horseradish peroxidase substrate was used to develop the color. Last, the signals were detected by ChemiDoc XRS+ Imaging System (Tanon, Shanghai, China). The ImageJ software was used for subsequent semiquantitative analysis. The integrated intensity of target protein divided by the integrated intensity of glyceraldehyde-3-phosphate dehydrogenase represented the relative expression of target protein.

Quantitative real-time polymerase chain reaction

Total RNA was extracted by using TRIzol reagent (15596018, Invitrogen, USA) according to the manufacturer's instructions. The concentration of RNA was determined by using NanoDrop (Thermo Fisher Scientific, USA). The reverse transcription was completed by using the corresponding kit (R323-01, Vazyme, Nanjing, China). The qPCR was performed by magnifying the diluted complementary DNA of 20 μl with the SYBR Green Q-PCR Kit (Q141-03, Vazyme, Nanjing, China) using the Applied Biosystems StepOnePlus Real-Time PCR System (Foster City, CA, USA). The gene expression was calculated using the $2^{-\Delta\Delta CT}$ and represented with fold change. The primer sequences were shown in table S4.

Human SMSCs immunofluorescence and semiquantitative analysis

Human SMSCs were fixed with 4% paraformaldehyde for 15 min and then permeabilized with PBS–Triton X-100 (0.1%) for 10 min at room temperature. The cells were blocked with 5% (w/v) BSA for 30 min at room temperature. Afterward, the cells were incubated with corresponding primary antibodies for 1 hour at 37°C. Then, the cells were incubated with a mixture of corresponding secondary antibodies, phalloidin and 4′,6-diamidino-2-phenylindole (DAPI) for 30 min. Last, the confocal microscope (Leica, Germany) was used to capture images. The integrated intensity of corresponding target was evaluated by ImageJ software (U.S. National Institutes of Health). In addition, the integrated intensity of nucleus (DAPI) was calculated. The intensity of corresponding target divided by the intensity of nucleus was calculated and compared.

Tissue immunofluorescence, immunohistochemistry, two-photon microscopy, semiquantitative analysis, and immunofluorescence colocalization coefficient

For tissue immunofluorescence, first, 3-μm-thick paraffin sections were prepared by using a microtome (Leica, Germany). The sections were immersed into xylene and graded ethanol to deparaffinize and regain water. The heat-induced antigen retrieval was completed using pH 6.0 citric acid for 20 min. The nonspecific protein binding was blocked using goat serum (Boster, AR0009, China) for 1 hour at room temperature. The sections were then incubated with the corresponding primary antibodies for 2 hours at room temperature and subsequently incubated with the corresponding secondary antibodies for 1 hour at room temperature, followed by DAPI incubation. Last, the confocal microscope (Leica, Germany) was used to capture images. The two-photon microscopy (TCS-SP8 DIVE, Leica, Germany) was used to acquire the second harmonic generation (SHG) signal associated with collagen matrix. The SHG signal was investigated with 850-nm excitation and 415- to 435-nm emission wavelength.

For semiquantitative analysis, the integrated intensity of corresponding target was evaluated by ImageJ software (U.S. National Institutes of Health, USA). For immunofluorescence colocalization coefficient, using the Coloc 2 plugin function of ImageJ software, the Manders colocalization coefficient was calculated.

Costaining of SOX9 immunofluorescence and biotin-labeled ISH for SRY gene

The probe for ISH of SRY gene was designed according to a previous study (*16*). Probe information is as follows: SRY probe (5′ and 3′ biotin) TGCAAGCAGCAAACTGTCGCT. The solutions during ISH are free of ribonuclease. The paraffin-embedded sections were immersed into xylene and ethanol to deparaffinize and regain water. The sections were permeabilized by proteinase K solution (20 ug/ml) at 37°C for 15 min and then washed with PBS. Then, the slices were treated with prehybridization buffer for 1 hour at 37°C. The tissue section was incubated with hybridization mix (hybridization buffer with SRY probe, 80 nM) for 1 hour at 54° C. After hybridization, rigorous wash was completed with graded sodium citrate buffer and PBS. Nonspecific protein binding was blocked by 1% BSA at room temperature for 15 min. Then, the tissue sections were incubated with fluorescein isothiocyanate–labeled anti-biotin and SOX9 antibody at room temperature for 1 hour. Last, the sections were incubated with secondary antibody and DAPI for 30 min and then sealed with antifluorescence-quenching sealing tablets after washing. The stained slices of ISH were scanned by confocal microscope (TCS-SP8, Leica). Using ImageJ software, selecting SRY-positive cells (green fluorescence), the intensity of SOX9 immunofluorescence divided by DAPI intensity was calculated.

Nanoindentation test

The nanoindentation test was performed according to a previous study (*61*). Briefly, the samples were harvested from the anterior, middle, and posterior portion of regenerated tissue or native porcine menisci. The samples were immersed into PBS solution to maintain hydration. The sample was glued to a glass slide with the surface vertical to the indentation direction. Care was taken to avoid sample drying or dehydration during the entire test process. A TriboIndenter (Hysitron) with a 400-μm radius curvature, conospherical, diamond probe tip was used. The random five points of each sample were tested. The trapezoidal load function with load (10 s), hold (2 s), and unload (10 s) was performed. The displacement control model with maximal 500 nm depth was used. Last, the reduced modulus was calculated after linear fitting to the load-displacement curve.

Intracellular Ca^{2+} concentration measurement

The intracellular Ca^{2+} concentration was measured using a Ca^{2+} probe, Fluo-4 AM (S1060, Beyotime, China). The SMSCs were incubated with 2 μM Fluo-4 AM for 20 min at 37°C. Then, the confocal microscope (Leica, Germany) was used to capture the immunofluorescence. The integrated intensity of calcium fluorescence was analyzed by ImageJ software.

RNA sequencing

We performed the human SMSCs and regenerated native porcine meniscal tissue RNA-seq analyses using Dr. Tom′s platform (https://biosys.bgi.com). The human SMSCs were treated with static or CTS. The regenerated tissue of PCL scaffold + synovium transplant group and native porcine menisci were harvested at the corresponding time point. Total RNA was extracted using TRIzol reagent. The cDNA libraries were constructed for each pooled RNA sample using MGIEasy RNA Directional kit Total RNA-seq. Bowtie2(v2.2.5) was applied to align the clean reads to the gene set. Expression level of gene was calculated by RSEM (v1.3.1). The gene expression was determined by transcripts per million (TPM) method. The differentially expressed genes were identified by DESeq2(v1.4.5) algorithm. Significant analysis was completed using the *P* value and false discovery rate (FDR) analyses. The genes with a fold change > 2 or fold change < 0.5 and FDR < 0.05 were considered to be differentially expressed. Gene Ontology (GO) analyses were used to clarify the biological implications of differentially expressed genes, including biological process, cellular component, and molecular function. To take insight to the change of phenotype, GO (http://geneontology.org/) and KEGG (https://kegg.jp/) enrichment analysis of annotated different expression gene were performed by Phyper (https://en.wikipedia.org/wiki/Hypergeometric_distribution) based on hypergeometric test. The significantly affected GO categories and pathways were identified by Fisher′s exact test. The *P* value was used to define the threshold of significance.

Statistical analysis

All data are presented as mean values ± SD. The data distribution is evaluated by Shapiro-Wilk test. The data are checked for equal variance before analysis. For the comparison of two groups, the unpaired two-tailed Student's *t* test is performed. For the comparison of multiple groups, the ordinary one-way analysis of variance (ANOVA) or two-way ANOVA with Bonferroni multiple comparison test is applied. A P value < 0.05 is considered statistically significant. All statistical analyses are completed using the GraphPad Prism software (version 8.0.1, GraphPad Software, USA).

Supplementary Materials

This PDF file includes:
Figs. S1 to S29
Legends for tables S1 to S93
Legends for movies S1 to S5

Other Supplementary Material for this manuscript includes the following:
Tables S1 to S93
Movies S1 to S5

REFERENCES AND NOTES

1. E. A. Makris, P. Hadidi, K. A. Athanasiou, The knee meniscus: Structure-function, pathophysiology, current repair techniques, and prospects for regeneration. *Biomaterials* **32**, 7411–7431 (2011).
2. S. Kim, J. Bosque, J. P. Meehan, A. Jamali, R. Marder, Increase in outpatient knee arthroscopy in the United States: A comparison of National Surveys of Ambulatory Surgery, 1996 and 2006. *J. Bone Joint Surg. Am.* **93**, 994–1000 (2011).
3. A. M. Seitz, A. Lubomierski, B. Friemert, A. Ignatius, L. Dürselen, Effect of partial meniscectomy at the medial posterior horn on tibiofemoral contact mechanics and meniscal hoop strains in human knees. *J. Orthop. Res.* **30**, 934–942 (2012).
4. H. Kwon, W. E. Brown, C. A. Lee, D. Wang, N. Paschos, J. C. Hu, K. A. Athanasiou, Surgical and tissue engineering strategies for articular cartilage and meniscus repair. *Nat. Rev. Rheumatol.* **15**, 550–570 (2019).
5. F. R. Noyes, S. D. Barber-Westin, Repair of complex and avascular meniscal tears and meniscal transplantation. *J. Bone Joint Surg. Am.* **92**, 1012–1029 (2010).
6. W. Yan, W. Dai, J. Cheng, Y. Fan, T. Wu, F. Zhao, J. Zhang, X. Hu, Y. Ao, Advances in the mechanisms affecting meniscal avascular zone repair and therapies. *Front. Cell Dev. Biol.* **9**, 758217 (2021).
7. J. C. Monllau, P. E. Gelber, F. Abat, X. Pelfort, R. Abad, P. Hinarejos, M. Tey, Outcome after partial medial meniscus substitution with the collagen meniscal implant at a minimum of 10 years' follow-up. *Arthroscopy* **27**, 933–943 (2011).
8. K. F. Schüttler, F. Haberhauer, M. Gesslein, T. J. Heyse, J. Figiel, O. Lorbach, T. Efe, P. P. Roessler, Midterm follow-up after implantation of a polyurethane meniscal scaffold for segmental medial meniscus loss: Maintenance of good clinical and MRI outcome. *Knee Surg. Sports Traumatol. Arthrosc.* **24**, 1478–1484 (2016).
9. Z.-Z. Zhang, Y.-R. Chen, S.-J. Wang, F. Zhao, X.-G. Wang, F. Yang, J.-J. Shi, Z.-G. Ge, W.-Y. Ding, Y.-C. Yang, T.-Q. Zou, J.-Y. Zhang, J. K. Yu, D. Jiang, Orchestrated biomechanical, structural, and biochemical stimuli for engineering anisotropic meniscus. *Sci. Transl. Med.* **11**, eaao0750 (2019).
10. C. H. Lee, S. A. Rodeo, L. A. Fortier, C. Lu, C. Erisken, J. J. Mao, Protein-releasing polymeric scaffolds induce fibrochondrocytic differentiation of endogenous cells for knee meniscus regeneration in sheep. *Sci. Transl. Med.* **6**, 266ra171 (2014).
11. C. M. Revell, K. A. Athanasiou, Success rates and immunologic responses of autogenic, allogenic, and xenogenic treatments to repair articular cartilage defects. *Tissue Eng. Part B Rev.* **15**, 1–15 (2009).
12. B. J. Ahern, J. Parvizi, R. Boston, T. P. Schaer, Preclinical animal models in single site cartilage defect testing: A systematic review. *Osteoarthr. Cartil.* **17**, 705–713 (2009).
13. K. Yamazaki, Y. Tachibana, Vascularized synovial flap promoting regeneration of the cryopreserved meniscal allograft: Experimental study in rabbits. *J. Orthop. Sci.* **8**, 62–68 (2003).
14. Y. Kobuna, K. Shirakura, M. Niijima, Meniscal repair using a flap of synovium. An experimental study in the dog. *Am. J. Knee Surg.* **8**, 52–55 (1995).
15. M. Kimura, K. Shirakura, A. Hasegawa, Y. Kobuna, M. Niijima, Second look arthroscopy after meniscal repair. Factors affecting the healing rate. *Clin. Orthop. Relat. Res.*, 185–191 (1995).
16. W. Yan, M. Maimaitimin, F. Zhao, Y. Fan, S. Yang, Y. Li, C. Cao, Z. Shao, Z. Liu, X. Hu, Y. Ao, J. Cheng, The transplantation of particulated juvenile allograft cartilage and synovium for the repair of meniscal defect in a lapine model. *J. Orthop. Transl.* **33**, 72–89 (2022).
17. Y. Sakaguchi, I. Sekiya, K. Yagishita, T. Muneta, Comparison of human stem cells derived from various mesenchymal tissues: Superiority of synovium as a cell source. *Arthritis Rheum.* **52**, 2521–2529 (2005).
18. H. Liu, X. Wei, X. Ding, X. Li, G. Zhou, P. Li, Y. Fan, Comparison of cellular responses of mesenchymal stem cells derived from bone marrow and synovium on combined silk scaffolds. *J. Biomed. Mater. Res. A* **103**, 115–125 (2015).
19. Y. Nakagawa, T. Muneta, S. Kondo, M. Mizuno, K. Takakuda, S. Ichinose, T. Tabuchi, H. Koga, K. Tsuji, I. Sekiya, Synovial mesenchymal stem cells promote healing after meniscal repair in microminipigs. *Osteoarthr. Cartil.* **23**, 1007–1017 (2015).
20. N. Ozeki, T. Muneta, S. Matsuta, H. Koga, Y. Nakagawa, M. Mizuno, K. Tsuji, Y. Mabuchi, C. Akazawa, E. Kobayashi, T. Saito, I. Sekiya, Synovial mesenchymal stem cells promote meniscus regeneration augmented by an autologous Achilles tendon graft in a rat partial meniscus defect model. *Stem Cells* **33**, 1927–1938 (2015).
21. D. J. Huey, K. A. Athanasiou, Tension-compression loading with chemical stimulation results in additive increases to functional properties of anatomic meniscal constructs. *PLOS ONE* **6**, e27857 (2011).
22. J. L. Puetzer, L. J. Bonassar, Physiologically distributed loading patterns drive the formation of zonally organized collagen structures in tissue-engineered meniscus. *Tissue Eng. Part A* **22**, 907–916 (2016).
23. D.-H. Lee, T.-H. Kim, J.-M. Kim, S.-I. Bin, Results of subtotal/total or partial meniscectomy for discoid lateral meniscus in children. *Arthroscopy* **25**, 496–503 (2009).
24. C. R. Chu, M. Szczodry, S. Bruno, Animal models for cartilage regeneration and repair. *Tissue Eng. Part B Rev.* **16**, 105–115 (2010).
25. K. Mizuno, T. Muneta, T. Morito, S. Ichinose, H. Koga, A. Nimura, T. Mochizuki, I. Sekiya, Exogenous synovial stem cells adhere to defect of meniscus and differentiate into cartilage cells. *J. Med. Dent. Sci.* **55**, 101–111 (2008).
26. R. E. Wilusz, J. Sanchez-Adams, F. Guilak, The structure and function of the pericellular matrix of articular cartilage. *Matrix Biol.* **39**, 25–32 (2014).
27. R. Schweizer, M. Waldner, S. Oksuz, W. Zhang, C. Komatsu, J. A. Plock, V. S. Gorantla, M. G. Solari, L. Kokai, K. G. Marra, J. P. Rubin, Evaluation of porcine versus human mesenchymal stromal cells from three distinct donor locations for cytotherapy. *Front. Immunol.* **11**, 826 (2020).
28. M. Freutel, A. M. Seitz, F. Galbusera, A. Bornstedt, V. Rasche, M. L. Knothe Tate, A. Ignatius, L. Durselen, Medial meniscal displacement and strain in three dimensions under compressive loads: MR assessment. *J. Magn. Reson. Imaging* **40**, 1181–1188 (2014).
29. X. Varelas, P. Samavarchi-Tehrani, M. Narimatsu, A. Weiss, K. Cockburn, B. G. Larsen, J. Rossant, J. L. Wrana, The Crumbs complex couples cell density sensing to Hippo-dependent control of the TGF-β-SMAD pathway. *Dev. Cell* **19**, 831–844 (2010).
30. T. Furumatsu, M. Tsuda, N. Taniguchi, Y. Tajima, H. Asahara, Smad3 induces chondrogenesis through the activation of SOX9 via CREB-binding protein/p300 recruitment. *J. Biol. Chem.* **280**, 8343–8350 (2005).
31. B. Dienes, T. Bazsó, L. Szabó, L. Csernoch, The role of the Piezo1 mechanosensitive channel in the musculoskeletal system. *Int. J. Mol. Sci.* **24**, 6513 (2023).
32. T. Parpaite, B. Coste, Piezo channels. *Curr. Biol.* **27**, R250–R252 (2017).
33. T. Zhou, B. Gao, Y. Fan, Y. Liu, S. Feng, Q. Cong, X. Zhang, Y. Zhou, P. S. Yadav, J. Lin, N. Wu, L. Zhao, D. Huang, S. Zhou, P. Su, Y. Yang, Piezo1/2 mediate mechanotransduction essential for bone formation through concerted activation of NFAT-YAP1-ß-catenin. *eLife* **9**, e52779 (2020).
34. T. P. Creamer, Calcineurin. *Cell Commun. Signal* **18**, 137 (2020).
35. C. R. Beals, N. A. Clipstone, S. N. Ho, G. R. Crabtree, Nuclear localization of NF-ATc by a calcineurin-dependent, cyclosporin-sensitive intramolecular interaction. *Genes Dev.* **11**, 824–834 (1997).
36. J. Aramburu, M. B. Yaffe, C. López-Rodríguez, L. C. Cantley, P. G. Hogan, A. Rao, Affinity-driven peptide selection of an NFAT inhibitor more selective than cyclosporin A. *Science* **285**, 2129–2133 (1999).
37. Z. Meng, Y. Qiu, K. C. Lin, A. Kumar, J. K. Placone, C. Fang, K. C. Wang, S. Lu, M. Pan, A. W. Hong, T. Moroishi, M. Luo, S. W. Plouffe, Y. Diao, Z. Ye, H. W. Park, X. Wang, F. X. Yu, S. Chien, C. Y. Wang, B. Ren, A. J. Engler, K. L. Guan, RAP2 mediates mechanoresponses of the Hippo pathway. *Nature* **560**, 655–660 (2018).
38. I. Dasgupta, D. McCollum, Control of cellular responses to mechanical cues through YAP/TAZ regulation. *J. Biol. Chem.* **294**, 17693–17706 (2019).
39. S. V. Eleswarapu, D. J. Responte, K. A. Athanasiou, Tensile properties, collagen content, and crosslinks in connective tissues of the immature knee joint. *PLOS ONE* **6**, e26178 (2011).

40. O. Maller, A. P. Drain, A. S. Barrett, S. Borgquist, B. Ruffell, I. Zakharevich, T. T. Pham, T. Gruosso, H. Kuasne, J. N. Lakins, I. Acerbi, J. M. Barnes, T. Nemkov, A. Chauhan, J. Gruenberg, A. Nasir, O. Bjarnadottir, Z. Werb, P. Kabos, Y. Y. Chen, E. S. Hwang, M. Park, L. M. Coussens, A. C. Nelson, K. C. Hansen, V. M. Weaver, Tumour-associated macrophages drive stromal cell-dependent collagen crosslinking and stiffening to promote breast cancer aggression. *Nat. Mater.* **20**, 548–559 (2021).
41. T. Panciera, A. Citron, D. Di Biagio, G. Battilana, A. Gandin, S. Giulitti, M. Forcato, S. Bicciato, V. Panzetta, S. Fusco, L. Azzolin, A. Totaro, A. P. Dei Tos, M. Fassan, V. Vindigni, F. Bassetto, A. Rosato, G. Brusatin, M. Cordenonsi, S. Piccolo, Reprogramming normal cells into tumour precursors requires ECM stiffness and oncogene-mediated changes of cell mechanical properties. *Nat. Mater.* **19**, 797–806 (2020).
42. F. S. Passini, P. K. Jaeger, A. S. Saab, S. Hanlon, N. A. Chittim, M. J. Arlt, K. D. Ferrari, D. Haenni, S. Caprara, M. Bollhalder, B. Niederöst, A. N. Horvath, T. Götschi, S. Ma, B. Passini-Tall, S. F. Fucentese, U. Blache, U. Silván, B. Weber, K. G. Silbernagel, J. G. Snedeker, Shear-stress sensing by PIEZO1 regulates tendon stiffness in rodents and influences jumping performance in humans. *Nat. Biomed. Eng.* **5**, 1457–1471 (2021).
43. F. Guilak, L. G. Alexopoulos, M. L. Upton, I. Youn, J. B. Choi, L. Cao, L. A. Setton, M. A. Haider, The pericellular matrix as a transducer of biomechanical and biochemical signals in articular cartilage. *Ann. N. Y. Acad. Sci.* **1068**, 498–512 (2006).
44. G. Gao, S. Chen, Y. A. Pei, M. Pei, Impact of perlecan, a core component of basement membrane, on regeneration of cartilaginous tissues. *Acta Biomater.* **135**, 13–26 (2021).
45. Y. Nakagawa, L. A. Fortier, J. J. Mao, C. H. Lee, M. B. Goodale, M. F. Koff, T. J. Uppstrom, B. Croen, S. Wada, C. B. Carballo, H. G. Potter, S. A. Rodeo, Long-term evaluation of meniscal tissue formation in 3-dimensional-printed scaffolds with sequential release of connective tissue growth factor and TGF-β3 in an ovine model. *Am. J. Sports Med.* **47**, 2596–2607 (2019).
46. W. E. B. Johnson, B. Caterson, S. M. Eisenstein, S. Roberts, Human intervertebral disc aggrecan inhibits endothelial cell adhesion and cell migration in vitro. *Spine* **30**, 1139–1147 (2005).
47. T. Kobayashi, I. Kakizaki, H. Nozaka, T. Nakamura, Chondroitin sulfate proteoglycans from salmon nasal cartilage inhibit angiogenesis. *Biochem .Biophys. Rep.* **9**, 72–78 (2017).
48. X. Tang, H. Muhammad, C. McLean, J. Miotla-Zarebska, J. Fleming, A. Didangelos, P. Önnerfjord, A. Leask, J. Saklatvala, T. L. Vincent, Connective tissue growth factor contributes to joint homeostasis and osteoarthritis severity by controlling the matrix sequestration and activation of latent TGFβ. *Ann. Rheum. Dis.* **77**, 1372–1380 (2018).
49. G. Zhen, Q. Guo, Y. Li, C. Wu, S. Zhu, R. Wang, X. E. Guo, B. C. Kim, J. Huang, Y. Hu, Y. Dan, M. Wan, T. Ha, S. An, X. Cao, Mechanical stress determines the configuration of TGFβ activation in articular cartilage. *Nat. Commun.* **12**, 1706 (2021).
50. T. Furumatsu, E. Matsumoto, T. Kanazawa, M. Fujii, Z. Lu, R. Kajiki, T. Ozaki, Tensile strain increases expression of CCN2 and COL2A1 by activating TGF-β-Smad2/3 pathway in chondrocytic cells. *J. Biomech.* **46**, 1508–1515 (2013).
51. R. Nakamichi, S. Ma, T. Nonoyama, T. Chiba, R. Kurimoto, H. Ohzono, M. Olmer, C. Shukunami, N. Fuku, G. Wang, E. Morrison, Y. P. Pitsiladis, T. Ozaki, D. D'Lima, M. Lotz, A. Patapoutian, H. Asahara, The mechanosensitive ion channel PIEZO1 is expressed in tendons and regulates physical performance. *Sci. Transl. Med.* **14**, eabj5557 (2022).
52. N. Ma, D. Chen, J. H. Lee, P. Kuri, E. B. Hernandez, J. Kocan, H. Mahmood, E. D. Tichy, P. Rompolas, F. Mourkioti, Piezo1 regulates the regenerative capacity of skeletal muscles via orchestration of stem cell morphological states. *Sci. Adv.* **8**, eabn0485 (2022).
53. A. Hupfer, A. Brichkina, A. Koeniger, C. Keber, C. Denkert, P. Pfefferle, F. Helmprobst, A. Pagenstecher, A. Visekruna, M. Lauth, Matrix stiffness drives stromal autophagy and promotes formation of a protumorigenic niche. *Proc. Natl. Acad. Sci. U.S.A.* **118**, e2105367118 (2021).
54. Y. Jiang, H. Zhang, J. Wang, Y. Liu, T. Luo, H. Hua, Targeting extracellular matrix stiffness and mechanotransducers to improve cancer therapy. *J. Hematol. Oncol.* **15**, 34 (2022).
55. Q. Li, F. Qu, B. Han, C. Wang, H. Li, R. L. Mauck, L. Han, Micromechanical anisotropy and heterogeneity of the meniscus extracellular matrix. *Acta Biomater.* **54**, 356–366 (2017).
56. L. A. Vonk, R. J. Kroeze, B. Z. Doulabi, R. J. Hoogendoorn, C. Huang, M. N. Helder, V. Everts, R. A. Bank, Caprine articular, meniscus and intervertebral disc cartilage: An integral analysis of collagen network and chondrocytes. *Matrix Biol.* **29**, 209–218 (2010).
57. L. Moroni, J. R. de Wijn, C. A. van Blitterswijk, Three-dimensional fiber-deposited PEOT/PBT copolymer scaffolds for tissue engineering: Influence of porosity, molecular network mesh size, and swelling in aqueous media on dynamic mechanical properties. *J. Biomed. Mater. Res. A* **75**, 957–965 (2005).
58. M. A. Sweigart, C. F. Zhu, D. M. Burt, P. D. DeHoll, C. M. Agrawal, T. O. Clanton, K. A. Athanasiou, Intraspecies and interspecies comparison of the compressive properties of the medial meniscus. *Ann. Biomed. Eng.* **32**, 1569–1579 (2004).
59. A. Vairis, G. Stefanoudakis, M. Petousis, N. Vidakis, A. M. Tsainis, B. Kandyla, Evaluation of an intact, an ACL-deficient, and a reconstructed human knee joint finite element model. *Comput. Methods Biomech. Biomed. Engin.* **19**, 263–270 (2016).
60. W. Yan, X. Xu, Q. Xu, Z. Sun, Q. Jiang, D. Shi, Platelet-rich plasma combined with injectable hyaluronic acid hydrogel for porcine cartilage regeneration: A 6-month follow-up. *Regen. Biomater.* **7**, 77–90 (2020).
61. W. Yan, X. Xu, Q. Xu, Z. Sun, Z. Lv, R. Wu, W. Yan, Q. Jiang, D. Shi, An injectable hydrogel scaffold with kartogenin-encapsulated nanoparticles for porcine cartilage regeneration: A 12-month follow-up study. *Am. J. Sports Med.* **48**, 3233–3244 (2020).

Acknowledgments: We thank X. Duan, X. Fu, and J. Zhang in the Institute of Sports Medicine of Peking University to perform technical support. **Funding:** This work was supported by the National Natural Science Foundation of China (nos. 82172420, 32000923, 82202723, and 81802161), Beijing Municipal Natural Science Foundation (no. 7214304), and Beijing Municipal Science and Technology Commission (no. Z171100001017085). **Author contributions:** W.Y. conducted most of the experiments, data collection, data analyses, and manuscript preparation. M.M., Y.W., and Y.F. conducted some of the surgery, data collection, and manuscript preparation. S.R. contributed to finite element analysis model construction and analysis. F.Z. and C.C. conducted some of cells related experiments, tissue histological analysis, and 3D printing. X.H., J.C., and Y.A. designed and supervised the whole project and wrote the manuscript. **Competing interests:** The authors declare that they have no competing interests. **Data and materials availability:** All data needed to evaluate the conclusions in the paper are present in the paper and/or the Supplementary Materials. The raw RNA-seq data generated in this study have been deposited in the National Center for Biotechnology Sequences Read Archive under accession code IDs PRJNA916640 and PRJNA916641.

Submitted 23 January 2023
Accepted 6 October 2023
Published 8 November 2023
10.1126/sciadv.adg8138